THE SIGNIFICANCE OF AN INTRINSIC MRI PARAMETER IN THE DIAGNOSIS OF MYOCARDIAL ISCHEMIA

Ph.D. Thesis by:
Pal Peter Kiss, M.D.

Head of the Doctoral School: Prof. Sámuel Komoly MD, DSc

Head of the Doctoral Program: Prof. Erzsébet Rőth MD, DSc

Supervisor: Prof. Tamás Simor MD, PhD

Heart Institute

University of Pécs, Pécs, Hungary

2010

TABLE OF CONTENTS

1 ABBREVIATIONS

BOLD MRI blood oxygenation level–dependent MRI

CA contrast agent

ceMRI contrast enhanced magnetic resonance imaging

DCE MRI dynamic contrast enhanced MRI

FID free induction decay

FOV field of view

Gd(ABE-DTTA) gadolinium (*N*-(2-butyryloxyethyl)-*N*¢-(2-ethyloxyethyl)-*N*,*N*¢-bis[*N*¢¢,*N*¢¢-bis(carboxymethyl)acetamido]-1,2-ethanediamine

IR inversion recovery

LAD left anterior descending (coronary artery)

MP myocardial perfusion

MRI magnetic resonance imaging

MRS magnetic resonance spectroscopy

NI neoplastic index

NI_v percent neoplastic index

NMRD Nuclear Magnetic Resonance Dispersion

NV neoplastic volume

PC prostate cancer

PIN prostate intraepithelial neoplasia

PM perfusion map

PPM percent perfusion map

PSA prostate specific antigen

R1 longitudinal relaxation rate

$R1_v$ R1 measured in any given voxel

ROI region of interest

SI signal intensity

SIE signal intensity enhancement

T1 longitudinal relaxation time

T2 transverse relaxation time

TI inversion time

TRAMP TRAnsgenic Mouse Prostate adenocarcinoma

v voxel

VBM virtual biopsy map

V_v voxel volume

WD well defined adenocarcinoma

WM wall motion

WT wall thickening

2 INTRODUCTION

2.1 CONTRAST AGENTS AND THEIR IMPORTANCE

MRI signal intensity is principally determined by proton relaxation rates (1/T1 and 1/T2). Thus, it provides the most useful clinical information when the relaxation rates are sufficiently different in healthy vs. diseased tissue. Unfortunately, often there are no sufficient intrinsic differences between the relaxation rates of healthy and diseased tissues. Paramagnetic metal ions, i.e. metal ions that possess unpaired electrons can enhance MRI signal intensity. Gadolinium (Gd^{3+}), one of the paramagnetic lanthanide metal ions, induces the largest relaxation rate enhancement. This enhancement is partially mediated by the direct interaction of the proton spins of water molecules in the inner coordination sphere of the paramagnetic metal ion (1,2).

The solubility of free lanthanide aquo-ions at physiological pH is limited. Also, lanthanide, aguo-ions are toxic, inducing cell apoptosis, probably due their effects on mitochondrial membranes (3). Organic chelator molecules with negatively charged carboxylate groups can form nontoxic and soluble complexes with Gadolinium. Such complexes are used as MRI contrast agents. Since contrast agents are distributed in body tissue by the blood circulation, differentially between healthy vs. diseased tissue, they can generate relaxation rate differences between the former and the latter, consequently effecting functional enhancement of contrast in MRI images.

2.2 SIGNIFICANCE OF R1 MEASUREMENT

To date, most of the MRI measurements in the clinic have been based on signal intensity (SI) images. In contrast enhanced MRI (ceMRI) the images show

tissue differentiation, when they do, on the basis of signal intensity enhancement (SIE). SIE in ceMRI is dependent on contrast agent concentration in the tissue volume element (voxel) represented by the image area in question, but not in a linear fashion. SI is not an intrinsic parameter, rather it is also dependent on the pulse sequence and acquisition parameters used. Another confounding factor is the inhomogeneity caused by the MRI coil, artificially imparting varying SIs to different parts of the prostate depending on their relative position to the coil. The intrinsic physical parameter which is enhanced in linear proportion with contrast agent concentration is the paramagnetic ΔR1 (longitudinal relaxation rate enhancement), induced by a contrast agent.(4) The R1 measurement, in the presence of a proper contrast agent, therefore, is not only a quantitative but a reproducible method to detect pathomorphologies.

2.3 CLINICAL APPLICATIONS

Contrast enhanced MRI is an important clinical tool in the management of patients with cardiac diseases. It allows clinicians to assess morphologic and physiologic myocardial characteristics in the same imaging session. Our results suggest that R1 mapping, eliminating the above detailed factors, may provide quantitative, reproducible information that can be used to follow up patients with myocardial perfusion defects.

It is highly desired to develop a non-invasive diagnostic tool to detect prostate cancer (PC) in its early phase. The presently used diagnostic methods (PSA, needle biopsy, etc) including DCE MRI, can only be used in the developed phase of PC. With our method, in the presence of Gd(ABE-DTTA), it was possible to quantitatively determine the volume of neoplastic mass in the prostate of TRAMP mice in the early, PIN phases.

3 AIMS

3.1 To determine that our contrast agent Gd(ABE-DTTA) has a signal enhancement capability in the entire magnetic field range we are planning to carry out our experiments

3.2 To determine whether R1 mapping method is capable to provide more information than signal intensity MRI images. To investigate this question we will use R1 mapping in a canine ischemia-reperfusion model. Addition to that, R1 mapping will be carried out in a pixel-by-pixel manner, providing the highest possible resolution of the actual MRI instrument used in the experiment.

3.3 To determine whether R1 mapping can provide detailed information similarly to the myocardial ischemia model, in more than one pathomorphologies, namely, in a mouse model of the prostatic neoplasia.

4 THE UNIQUE R1 CHARACTERICTICS OF GD(ABE-DTTA)

4.1 INTRODUCTION

The agent Gd-ABE-DTTA (Fig1) has been developed in our laboratory (5).

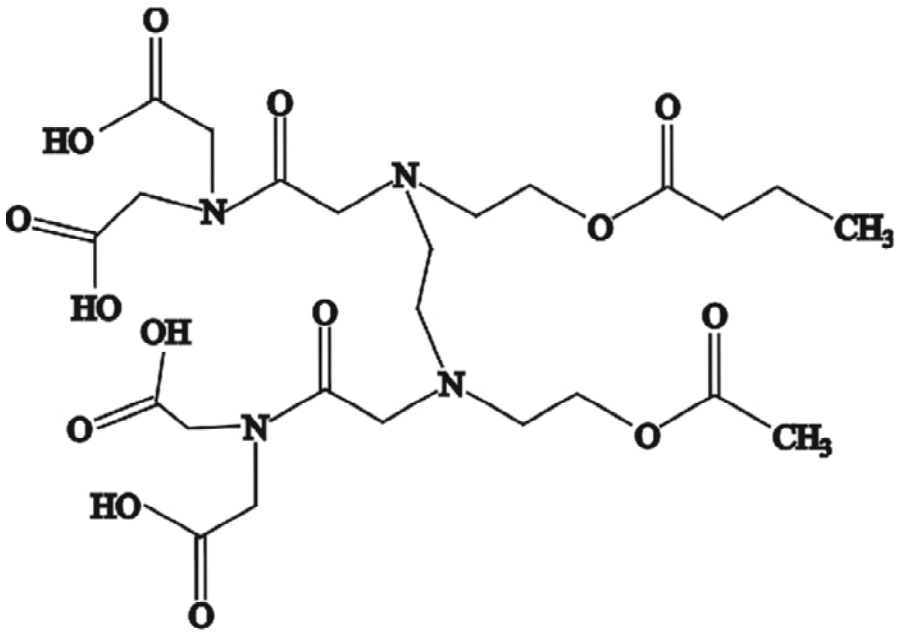

(ABE-DTTA)

Figure 1. The molecular scheme of the (ABE-DTTA) ligand.

In a canine model of acute ischemic underperfusion, we have used Gd(ABE-DTTA) successfully to detect ischemic defects in the myocardium not only at the extreme limit (100% left anterior descending (LAD) coronary artery occlusion) but also in partially underperfused myocardial experimental models (5,6). In recent studies, we have also used it to detect myocardial infarction (7). It has shown no deleterious physiological effects at the level of the MRI-effective dose in the canine model (8). The magnetic field dependence of the longitudinal relaxivity of this agent, particularly at high and very high fields (3-14 T) showed unique characteristics.

Thus for instance, MRI, enhanced by an appropriate contrast agent, makes possible the early and non-invasive detection of myocardial tissue underperfusion (9) (10) (11) (6).

Long Half Life in Blood and Tissue

According to our earlier results, Gd(ABE-DTTA) has a uniquely long life time in blood and tissues that makes often time consuming R1 assessment possible.

4.2 MATERIALS and METHODS

Gd(ABE-DTTA) was synthesized, and sample preparation was carried out, as described by Saab-Ismail et al [15]. Solutions of 1:1 Gd : ABE-DTTA and 0.7:0.7 Ca : ABE-DTTA were mixed to obtain a 10 mM (per Gd complex) stock. An amount of this stock was diluted to prepare a 0.1 mL (0.5 mM) sample. This sample was placed in a 1.5 mm O.D. tube inserted coaxially within a 5 mm O.D. NMR tube which contained CD_3Cl for locking purposes when a spectrometer was used to determine relaxivity. For measurements carried out on MRI scanners, a phantom was created with three vials, each containing 0.5 mM Gd(ABE-DTTA). The interior of the phantom around the vials was filled up with agarose.

All measurements, including the NMRD measurement, were carried out on 20 Cº.

In the range 0.0002-1.0T, the field dependence of the longitudinal relaxivity of Gd(ABE-DTTA) was assessed with NMRD as detailed by Koenig and Brown [18]. At field strengths above 1T a variety of single-field MRI instruments (1.5T GE CVI System, Bruker Biospec 4.7T) and NMR spectrometers (Bruker ARX 300, Bruker AM 360, Bruker DRX 400, Bruker DRX 500, Bruker DRX 600) were used.

On the 1.5T GE CVI System a segmented, inversion-recovery, fast-gradient-echo sequence was used to generate images with varying inversion-times. The imaging parameters were: FOV=300mm, image-matrix=256x256, slice-thickness=10mm, flip-angle=25°, echo-time (TE) = 3.32ms, views-per-segment=16, recycle-time(TR)= 3-5000ms (depending on the heart rate of a volunteer).

On the Bruker Biopac 4.7T MRI scanner a multi-slice multi-echo (msme) inversion recovery (IR) sequence was used for to acquire T1 values with the following parameters: FOV: 5 cm, matrix: 128·128, voxel size: 0.39mm·0.39mm·2mm (slice thickness), number of slices: 1, recycle time was 3000ms.

On the NMR spectrometers an inversion recovery sequence was used. The sequence parameters and magnetic field strength along with the inversion delay times used on the individual instruments are listed in Table 1.

In the experiments using an NMR spectrometer the R1 values were calculated from the signal intensities by the WINNMR software running on the individual NMR instrument using the Equation 1.

$$I_{(t)}=I_{(0)}+A\cdot\exp(-\tau/T_1) \qquad (1)$$

where $I_{(t)}$ is the measured intensity and τ is the interpulse delay time. $I_{(0)}$, A and T_1 were the variable parameters of the three parameter curve fitting. In the experiments carried out on MRI instruments, the images, acquired with different TIs, were exported to a PC computer as image stacks. They were reformatted using ImageJ (Wayne Rasband, NIH). Regions of interest were determined in the image stacks and the signal intensity value series were exported to Origin 6.1.

Table 1 Inversion Delay Times Used

System	GE CVI System	Bruker Biospec 4.7	Bruker ARX 300	Bruker AM 360	Bruker DRX 400	Bruker DRX 500	Bruker DRX 600
Field Strength (T)	1.5	4.7	7.1	8.5	9.4	12	14
Operating System	GE OS 8.1	3.1	XWINNMR 2.5	XWINNMR 2.5	XWINNMR 2.5	XWINNMR 3.5	XWINNMR 3.5
τ (ms)	35	10	1	0.5	1	0.1	0.1
	40	20	2	1	2	1	1
	50	30	4	100	4	5	5
	60	50	6.5	25	6.5	10	10
	70	70	10	50	10	30	30
	80	90	20	200	20	60	60
	90	100	40	500	40	120	120
	100	150	65	1000	65	250	250
	110	200	100	1500	100	500	500
	120	300	200	3000	200	1000	1000
	130	600	400		400	4000	4000
	140	1000	650		650	10000	10000
	160		1000		1000		
	180		1500		1500		
	220		2000		2000		
	260						
	280						
	300						
	600						
	1100						

Since these MR images are magnitude images, the polarity of the signal intensity values acquired with TIs less than the τ_0 value, had to be changed by the observer. Calculations were carried out in Origin 6.1, using Equation 1 for curve-fitting.

The relaxation rate enhancement, ΔR_1, induced by the contrast agent, was obtained from

$$\Delta R_1 = 1/T_{1\,(obs)} - 1/T_{1\,(o)} \qquad (2)$$

where $T_{1\ (obs)}$ was the observed water proton relaxation time in a solution with the contrast agent, and $T_{1\ (o)}$ was the relaxation time of pure water. In turn, the relaxivity r_1 was calculated from

$$r_1=\Delta \cdot R_1/c \qquad (3)$$

where c was the concentration (in mM) of the contrast agent.

4.3 RESULTS

In Figure 2, relaxivity values measured on the NMRD machine (Fig. 2A) and seven different single-field instruments (Fig. 2B) are plotted as a function of magnetic field strength. Similarly to other contrast agents, GD(ABE-DTTA) (molecular weight=760) shows its maximum relaxivity at magnetic field strengths less than 0.01 T, with a high relaxivity value, above 30 $s^{-1}mM^{-1}$, unusual for a small molecular weight agent, and which is only found with macromolecular complexes (67), (68).

Its relaxivity reaches a local minimum (~19 $s^{-1}mM^{-1}$) around 0.2-0.3 T (Fig. 2A). In distinction from the typical agents presently used in the clinic, its relaxivity increases with field strength above this point, reaches a local maximum around 5T (Fig 2B), and starts decreasing. Nevertheless, even at 8.5 T it is not lower than its relaxivity at 1.5 T.

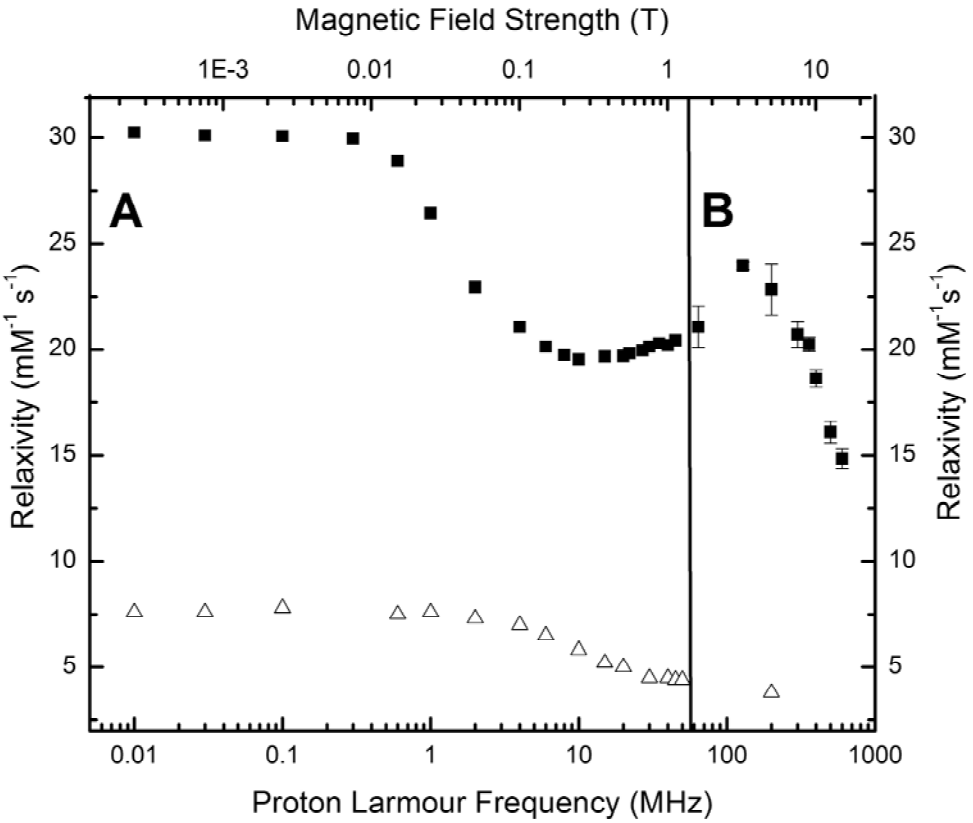

Figure 2 Field Dependecy Profile of the longitudinal relaxivity of Gd(DTPA) and Gd(ABE-DTTA) **Figure 2 (A)** The relaxivities (■) of 0.5 mM aqueous solutions of Gd(ABE-DTTA) and of Gd(DTPA) (Δ) acquired with NMRD as a function of magnetic field strength. The Gd(DTPA) NMRD data were adapted from Kellar et al. (70). The measurements of Gd(ABE-DTTA) were carried out at 20 ºC whereas the measurements of Gd(DTPA) were carried out at 25 ºC. **Figure 2 (B)** The relaxivity at 20 ºC of Gd(ABE-DTTA) (■) (n=12) and Gd(DTPA) carried out on a series of single field MRI and NMR instruments detailed in Table 1 as a function of magnetic field strength. The 4.7T datapoint for Gd(DTPA) (Δ), was adapted from Mikawa et al. (71). This study was carried out at 25 ºC.

At the most widespread magnetic field presently used in clinical practice, 1.5 T, the relaxivity was 21.5 $s^{-1}mM^{-1}$, a value considerably larger than that of presently used contrast agents. As the field increases, the relaxivity of Gd(ABE-DTTA) further increases, reaching a peak of almost 24 $s^{-1}mM^{-1}$ in the vicinity of 3T. It is noteworthy that even around 10T, the relaxivity is still at the considerably high level of 18.5 $s^{-1}mM^{-1}$. The relaxivity values measured on separate instruments, and shown in Figure 2B, are listed in Table 2.

Table 2. The relaxivity values of Gd(ABE-DTTA) measured on MRI and NMR instruments are shown along with corresponding field strength/proton Larmour frequency.

	Relaxivity Values		
Field Strenth (T)	^{1}H Larmour Frequency (MHz)	**Relaxivity ($mM^{-1}s^{-1}$)**	Standard Deviation
1.5	64	**21.07**	±0.97
3	128	**23.96**	±0.17
4.7	200	**22.83**	±1.21
7.1	300	**20.71**	±0.62
8.5	360	**20.24**	±0.34
9.4	400	**18.64**	±0.41
12	500	**16.10**	±0.50
14	600	**14.84**	±0.46

4.4 CONCLUSIONS

To emphasize the different field dependency profile of the Gd(ABE-DTTA) relaxivity compared to that of Gd(DTPA), both are shown in Figures 2A and 2B, with the Gd(DTPA) data adapted from Kellar et al (70) (Figure 2A) and Mikawa et al (71) (Figure 2B). The field dependence of the relaxivity of Gd^{3+} chelates is governed by numerous factors having complex relationships with each other, namely the inner coordination environment of the Gd^{3+} ions and the number of water molecules surrounding the Gd^{3+} in the inner sphere ; the field dependent electronic relaxation time of the unpaired electron spins (τ_S) of the Gd^{3+} magnetic moment, with low field limit (τ_{SO}),; the diffusional correlation time (τ_V) that describes the dependence of τ_s on magnetic the static field; the average distance between the Gd^{3+} and the water molecules in the inner sphere; the proton residence time (τ_M) of the coordinated water molecules, the diffusional time (τ_D) of a solvent water molecule in the outer sphere; and most likely the rotational correlation time of the Gd-chelate (72). The role of the

second hydration shell can be important when the ligand exchange in the inner sphere is slow (68). The field dependence profile of Gd(ABE-DTTA) looks qualitatively similar to those of the water solutions of protein-bound paramagnetic ions, for example Mn-concavalin A and Cu-SOD, reported by Koenig et al (67), (68). These authors interpreted the local maximum seen in the high field range for these complexes in terms of the relaxation properties of the electron spins of the paramagnetic ions, which manifest themselves in the proton relaxation through their contribution to the correlation time (67). The rotational correlation time (τ_R) is an additional important factor leading to a local maximum in relaxivity of some slowly-rotating Gd^{3+} complexes in the high field range (73). Toth et al investigated the NMRD profiles of gadofullerenes and also found a local relaxivity maximum in the high field range.

The field dependency profile of the Gd(ABE-DTTA) relaxivity is similar to the above mentioned high molecular weight complexes. Thus one would expect the environment of its Gd^{3+} ion to be similar to those of such slowly-rotating complexes. As Gd(ABE-DTTA) is of the relatively low molecular weight of 760 Dalton, its relaxivity profile is perplexing. We suggest that the chemical structure of the ABE-DTTA ligand (Fig. 1), with its lipophylic butyryl chain, may provide the explanation. Such lipophylic chains may lead to micelle formation, increasing the effective radius of the aggregate complex, and leading to the observed field dependency profile. Irrespective of the exact mechanism of its relaxivity, considering the historic trend of the development of clinical MRI instruments that operate at increasingly higher magnetic fields, Gd(ABE-DTTA) could become the contrast agent of choice in cases where high field imaging would be particularly useful.

5 IN VIVO R1-ENHANCEMENT MAPPING OF CANINE MYOCARDIUM USING CEMRI WITH GD(ABE-DTTA) IN AN ACUTE ISCHEMIA-REPERFUSION MODEL.

5.1 INTRODUCTION

Ischemic heart disease remains the leading cause of death in western societies (12). A non-invasive imaging method to visualize acute myocardial ischemia is highly desirable (13-15). The techniques currently used, contrast-enhanced cardiac ultrasound and technetium-99m-tetrofosmin Single-Photon Emission Computed Tomographic (SPECT) imaging, along with thallium-201 myocardial tomography, are not optimal for accurate localization and, more importantly, for quantitative determination of myocardial underperfusion (16). Presently, coronary angiography provides the most accurate information for the differential diagnosis of acute myocardial ischemia. This method, however, carries significant risks and is not repeatable as many times and as often as MRI is (17,18). Contrast-enhanced MRI (ceMRI) can visualize myocardial ischemia with less risk (19,20), but the present techniques of cardiac ceMRI could be improved on in the area of spatial resolution and coverage. In this work we present results obtained by R1 mapping, which in conjunction with a long tissue-lifetime contrast agent (CA), Gd(ABE-DTTA), provides quantitative pixel-by-pixel information on myocardial underperfusion.

In differential diagnosis of acute myocardial ischemia, cardiac MRI has played an increasingly important role in the visualization of perfusion abnormalities. Using BOLD MRI, myocardial ischemia can be detected without using contrast agents (21). However, to precisely delineate the ischemic area in the myocardium, the use of MRI contrast agents is required (22-24). Based on the distribution differences of a CA

between healthy and ischemic regions, ceMRI using gradient echo sequences should be able to detect and accurately assess myocardial underperfusion.

McNamara et al. used Gd-DTPA to detect myocardial ischemia in a canine heart model(25). Gd-DTPA has since remained the most frequently used MRI contrast agent for the detection of acute myocardial ischemia in clinical practice (26), although some investigators have used other agents in their experimental and human studies (27-32).

MRI contrast agents display wash-in and wash-out kinetics that reflect myocardial perfusion abnormalities (33). The application of a first-pass technique to detect myocardial ischemia in a rat heart model was reported by Atkinson et al. (34). The same authors also visualized myocardial ischemia in patients with coronary disease by first pass kinetics using Gd-DTPA (35). To date, this is the best MRI technique to detect myocardial perfusion (35). First pass techniques, however, are not optimal in spatial resolution and coverage due to short duration of contrast.

The signal intensity enhancement (SIE) is dependent on CA concentration in the myocardial volume element represented by the corresponding image area, but not in a linear fashion. SIE is not an intrinsic parameter, but is rather dependent on the pulse sequence and the acquisition parameters used. The intrinsic physical parameter which is enhanced in linear proportion with CA concentration is the paramagnetic relaxation rate enhancement, $\Delta R1$, which is the difference between the inverse T1 in presence versus absence of CA. Using $\Delta R1$ for the determination of regional CA concentration liberates this determination from dependence on extraneous experimental factors (field inhomogenities, preparation pulse errors, saturation, coil effect, etc.). The $\Delta R1$ obtained from an ROI that represents a given myocardial volume element actually represents the CA concentration integrated over that volume

element, because the R1 values, contrary to those of other parameters, are additive. Thus, a three dimensional (3D) ΔR1 map of the heart in ceMRI is a faithful representation of CA distribution with a spatial resolution down to the voxel-by-voxel level.

To benefit most from ceMRI, several techniques were developed to investigate myocardial perfusion defects (36) and pathologies in brain (37). First-pass, the commonly used technique to detect myocardial perfusion defects in patients, was first reported in 1991 (35). The accuracy of perfusion detection with this method, however, is limited since it utilizes MRI signal intensities. Since the signal intensity of a given pixel in an MRI image may be distorted by the factors detailed above, a signal-intensity-based image of the myocardium following CA administration may provide inaccurate quantitative information about the location and severity of myocardial underperfusion. Thus an R1-map-based approach would be preferable. Unfortunately, however, with MRI instruments presently used in the clinic, the acquisition of images using inversion recovery (IR) for a typical R1 map currently requires 15 minutes of scanning time per tomographic slice. Thus, the myocardial life-time of CAs presently used in the clinic is too short for obtaining a R1 map of the left ventricle (LV) with IR. To solve this problem, we have introduced an agent that remains in tissue long enough to allow the generation of a R1 map.

We had previously developed Gd(BME-DTTA), a tissue-persistent myocardial CA. Subsequently, we successfully applied it in a ferret myocardial ischemia model (38). Due to its relatively long life-time in the myocardium, the contrast between the ischemic and non-ischemic regions remained significant during the entire 30-minute ischemic period. Our present, related agent, Gd(ABE-DTTA) (5) (Fig. 1), has retained the MRI qualities of Gd(BME-DTTA), but it is preferable over the latter due to its

improved water solubility. It has been successfully used in our previous studies to detect myocardial underperfusion (39), (40). Its relatively long lifetime in the myocardium allows its use for R1 mapping of the entire LV.

5.2 MATERIALS and METHODS

Canine Preparation

Eleven male mongrel dogs weighing 17-19 kg were used in our study. An AcqKnowledge v3.7.2 software running on a Toshiba notebook PC, connected to a MP100A (Biopac Systems Inc., CA) were used to record ECG and pressure. Anesthesia was initiated with an initial I.V. bolus of sodium pentobarbital (25mg/kg). Dogs were intubated and mechanically ventilated. Body temperature was maintained. An I.V. line was inserted to administer infusion and Pentobarbital. Both femoral arteries were cannulated to obtain arterial blood samples during microsphere injections and to monitor blood pressure. Blood pressure and ECG were continuously recorded. A left side thoracotomy was performed. A 1 cm long section of the left ascending coronary artery (LAD) was isolated from its bed. A silk tie was placed around the LAD to allow occlusion during the ischemia. The aperture of the thoracotomy was closed to restore roughly a normal anatomical situation. To ascertain whether the size of the ischemic region was large enough, a 20 second zero-flow ischemia test was performed, monitored by ECG.

Experimental Protocol

Control short axis MRI images were acquired, microspheres of the first color were injected and a blood sample was taken. Subsequently, zero-flow ischemia was created by pulling the ligature tight and the contrast agent was injected. At that time, microspheres of the second color were injected, a blood sample was taken and from

the tenth minute throughout the thirtieth minute of the ischemic period cine and IR MRI images were collected. At the end of the thirty minute period of ischemia, the LAD ligature was removed to allow forty minutes of reperfusion. Microspheres of the third color were injected in the sixth minute of the reperfusion period and a blood sample and MRI images were taken. At the end of the reperfusion period the animal was euthanized. In Figure 3 the time line of our experimental protocol is illustrated (Fig.3).

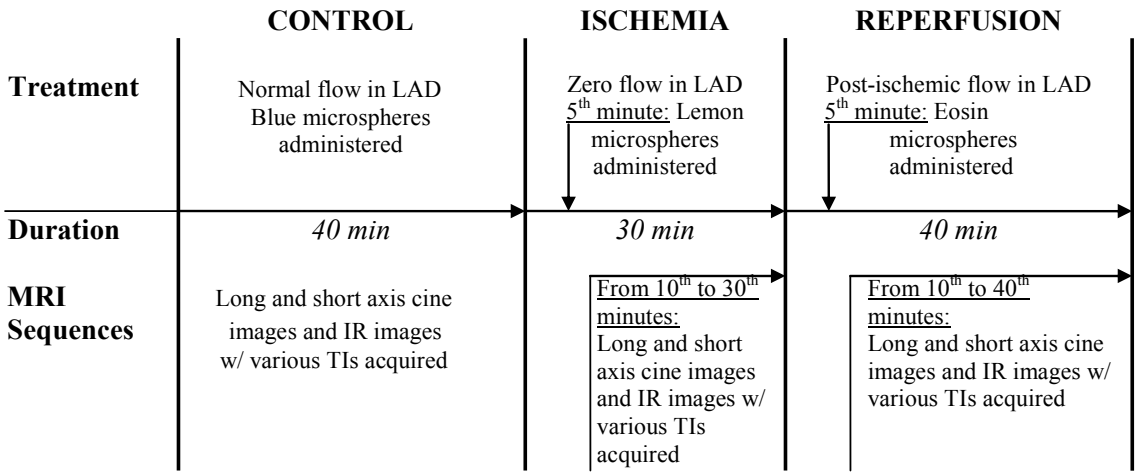

Figure 3 Timeline of the experimental protocol. Left anterior descending coronary artery: LAD, inversion recovery (IR), inversion time (TI).

Analysis of Microsphere Perfusion

The heart was excised, washed, and bread sliced according to the anatomical orientation of the short axis MRI images (see below). Each slice was cut into 8 or 16 pieces (depending on the mass of the actual slice) of approximately 1 gram each. Each tissue sample was placed individually in a test tube that contained 1M KOH for digestion at 60 °C for 12 hours. The blood samples, however, were digested by 2M KOH. Further processing of tissue and blood samples was carried out as described by

Simor et al (38) to calculate myocardial perfusion determined by colored microspheres (MP).

Contrast Agent

Agent Preparation:

Gd(ABE-DTTA) (Figure 1) was synthesized, and sample preparation was carried out as described by Saab at al. Each injectable sample of Gd(ABE-DTTA) was prepared by mixing solutions of Gd(ABE-DTTA) and Ca(ABE-DTTA) in a 10:3 ratio. For quality control, relaxivity of each such sample was measured, and a relaxivity of 16.2 $sec^{-1} \cdot mM^{-1}$ (pH 6.4; 20 °C) was routinely obtained.

Determination of Relaxivity: This determination was carried out for each injectible sample of CA to maintain quality control. The IR method was used to measure T1. A 180 degree preparation pulse was followed by a variable delay. The magnetization then was sampled by a second pulse and acquisition of the resulting free induction decay signal was carried out. Magnetization M_τ for any interpulse delay time τ is given by the equation:

$$M_\tau = M_{eq}(1-A^{-R1 \cdot \tau}) \qquad \text{(Eq 1)}$$

where M_{eq}, and R1 are the magnetization at equilibrium and the relaxation rate (R1 = l/T1), respectively. A is a constant dependent on the quality of the 180 degree pulse and the extent of signal saturation. Under ideal conditions, A = 2.0. For a series of delay times τ, FID intensities, or resonance intensities when Fourier Transformation is done, are generated and the data are fit to a curve described by Equation 1. A three-parameter, no-constraint fit is carried out and the R1, i.e., the relaxation rate, is obtained from the best fit. These measurements were carried out on an Avance (360 MHz, 8.5T) Bruker NMR spectrometer. For each sample, 1/T1 is calculated from three consecutive T1 measurements.

MRI

Slice Orientations

A 7 slice short axis image grid was positioned on the end diastolic image of a four chamber long axis steady-state-free-precession (SSFP) movie. The seven short axis tomographic slices were positioned starting from the level of the aortic valve. Slice thickness was chosen so that the seven slices would cover the entire left ventricle from apex to base. Since the duration of the 30 minute ischemia was insufficient to cover the entire LV, based on the anatomic position of the ligature of LAD only one of these seven slices was chosen to determine R1. Cine MRI, however, was acquired covering the entire LV.

Normalized ΔR1 mapping

An IR prepared segmented fast gradient echo sequence was used on a 1.5 Tesla GE Signa Horizon CV instrument to determine R1. R1 values were obtained using the IR method employing eight different TI values. Short axis IR images were obtained with the following parameters: 260 mm FOV, 256x256 image matrix, 25° read out flip angle, 3.32 ms echo time (TE). TR was determined by the actual heart rate (TR=3 cardiac cycles). The acquisition of all TIs was timed to end-diastolic phase of the cardiac cycle.

The R1 values for each region of interest (ROI) were calculated by curve fitting from the TI-dependent signal intensities using Equation 2 (60):

$$SI = SI_o\,(1 - A \cdot e^{-TI \cdot R1} + e^{-TR \cdot R1}) \qquad \text{(Eq 2)}$$

Where SI stands for observed signal intensity, SI_0 for signal intensity at equilibrium, TI for inversion time, TR for repetition time, and A is a parameter ($A \leq 2$) obtained by the curve fitting procedure. The rightmost exponential term corrects for signal saturation (60).

Two alternative post-acquisition calculations with two different spacial resolutions were both carried out: a) R1 values were calculated for each myocardial sector serving as ROI according to the physical sectors in which myocardial perfusion was determined using microspheres; and b) R1 values were also calculated with a voxel-by-voxel resolution (each voxel as an ROI) exploiting the maximum spatial resolution potential provided by the equipment and the imaging pulse sequence.

Myocardial Function

To determine myocardial function, cine MRI images were acquired using an SSFP sequence. The applied parameters were: 260 mm FOV, 128x128 image matrix, 45 ° flip angle.

Image Analysis

MR Analytical Software System (MASS) Version 5.0 (Medis, Leiden, Netherlands) running on a HP Pavilion 9600 PC was used for image analysis. The entire image set of a single study was scaled and windowed simultaneously. The corresponding signal intensity values of a set of IR images with varying TIs were used to determine R1 values of the myocardial ROIs. Myocardial function was determined using data calculated from SSFP movies. Following the localization of the centerpoint, the endo- and epicardial contours of the LV muscle in the short axis images were detected and manually readjusted. A 0^{o} starting point at the postero-septal groove is set for each individual image in the set. Following these initial settings, the software divided the mass of the LV muscle into 16 segments where each individual segment was perpendicular to the centerline.

Function and ΔR1 Data Analysis:

The MASS program calculated cardiac function data, such as the difference between the end systolic and end diastolic wall thickness, wall thickening (WT); and the displacement of the end-systolic endocardial contour, wall motion (WM). Signal intensity (SI) data for each ROI were also measured using MASS. WT and MRI SI data were derived from the same myocardial volume elements. Corresponding data tables of WT and SI were then generated for the entire image set and processed. An R1 value was calculated for each individual ROI, thus generating an R1 map. An R1 enhancement ($\Delta R1_{ca}$) as defined by Eq 3, induced by CA in a given pixel, is proportional to the concentration of the CA in the voxel represented by that pixel.

$$\Delta R1_{ca} \sim R1_0 \bullet [CA] \qquad \text{(Eq 3)}$$

Where $R1_0$ is the precontrast R1. This concentration is perfusion dependent, and thus the ΔR1 value of a given pixel is proportional to the perfusion in its voxel. The observed relaxation rate ($R1_{obs}$) of a given pixel in the presence of the CA is the sum of the control relaxation rate $R1_0$ obtained in the absence of the CA and the relaxation rate enhancement $\Delta R1_{ca}$ induced by the CA. Therefore,

$$\Delta R1_{ca} = R1_{obs} - R1_0 \qquad \text{(Eq 4)}$$

In comparison with corresponding MP values, sectors with ΔR1 less than or equal to 0.8 s^{-1} were considered representing ischemic ROIs ($\Delta R1_{cai}$). Thus, sectors with ΔR1 values larger than 0.8 s^{-1} represented non-ischemic, remote sectors ($\Delta R1_{car}$).

To eliminate differences in R1 data among the individual dogs due to potential differences in effective contrast agent tissue uptake, all ΔR1 values were normalized to the average of the ΔR1 values observed in the non-ischemic areas ($\Delta R1_{car}$) in each individual dog.

$$\Delta R1_n = \Delta R1_{cai} / [\Delta R1_{car}] \qquad \text{Eq(5)}$$

The calculated values were compiled as a function of anatomical position. These normalized $\Delta R1_n$ data from all ROIs in a given dog constitute the R1-enhancement map ($\Delta R1_n$) which represents the myocardial perfusion distribution.

Regional Function Analysis:

A regional function map corresponding to the $\Delta R1_n$ map was generated. Myocardial function of each individual sector was also compared to the corresponding myocardial perfusion and $\Delta R1_n$ data.

Pixel-by-pixel Image Analysis:

To determine the $\Delta R1_n$ values in the myocardium with a higher spatial resolution, a series of eight superimposable 60 pixel by 60 pixel image sections, containing the LV, was selected from the MRI images acquired with the eight different TIs. An automated algorithm was applied to determine the R1 value in each voxel associated with each pixel, using Equation 2.

Perfusion Map:

The relaxation rate, consequently the $\Delta R1_n$, of a given pixel is proportional to the concentration of the CA. This concentration is perfusion dependent, and thus the $\Delta R1_n$ value of a given pixel is proportional to the perfusion. Based on this correlation, the pixel-by-pixel $\Delta R1_n$ map can be transformed into a pixel-by-pixel perfusion map (PM).

Percent Perfusion Map (PPM):

To establish a scale to convert $\Delta R1_n$ values to perfusion values, the pixel with the maximum $\Delta R1_n$ value ($\Delta R1_{nmax}$) in that myocardium is sought. To calculate the exact percent perfusion value in each individual voxel, the following derivation applies:

$$\Delta R1_{nmax} \sim \text{Perfusion}_{max}$$

$$\Delta R1_{nmin} \sim Perfusion_{min} \quad \text{(Eq 6)}$$

$$\Delta R1_n \sim Perfusion$$

$$\Delta R1_n / \Delta R1_{nmax} = Perfusion / Perfusion_{max}$$

$$Perfusion = (\Delta R1_n / \Delta R1_{nmax}) \bullet Perfusion_{max} \quad \text{(Eq 7)}$$

Thus, to express the perfusion in any given voxel as a percent of the maximum perfusion in a particular LV, a Percent Perfusion (PP) parameter is calculated from Eq 5:

$$PP = (\Delta R1_n/\Delta R1_{nmax}) \bullet 100 \quad \text{(Eq 8)}$$

The matrix containing the PP values of all voxels then yields the Percent Perfusion Map (PPM).

Statistical analysis

Data were analyzed using SigmaStat version 3.0 (SPSS, Inc). Details of the statistical analysis for each type of results are given in the Results section.

5.3 RESULTS

In Figure 4 are depicted the mean ± standard error of $\Delta R1_n$ values calculated in ischemic (n=47) and non-ischemic sectors (n=94) of the eleven dogs. Using normalized ΔR1 values (see METHODS section) all the $\Delta R1_n$ values obtained in the 11 dogs were made animal-independent and thus comparable. Following CA administration, during the

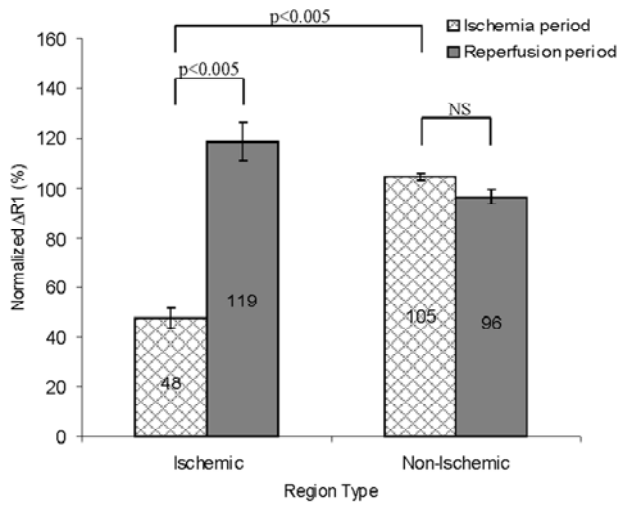

Figure 4 Average ΔR1 values of the ischemic and non-ischemic sectors normalized to theR1 values measured during the control period in the corresponding sectors.

ischemia period a significant $\Delta R1_n$ difference was found between the ischemic and non-ischemic ROIs by using Mann-Whitney Rank test ($p < 0.001$). Upon reperfusion, the difference not only decreased, but due to likely hyperemia and a consequently higher CA concentration in the previously ischemic myocardium, the $\Delta R1_n$ value increased in these areas compared to the non-ischemic areas. This difference, however, was not significant.

A typical image set from which $\Delta R1_n$ values were obtained is shown in Figure 5. These images of a single LV tomographic slice were acquired with the eight different TIs. In images acquired with TIs below the contrast reversal point, reverse contrast is observed between the well perfused and ischemic regions; the ischemic region is brighter than the non-ischemic regions. The minimum signal intensities occurred around 400 ms for both the ischemic and non-ischemic regions. At TIs above 400 ms, the contrast becomes positive, i.e. the ischemic region is darker and the well-perfused region is brighter. The maximum contrast is observable in images acquired with TIs between 600 and 900 ms.

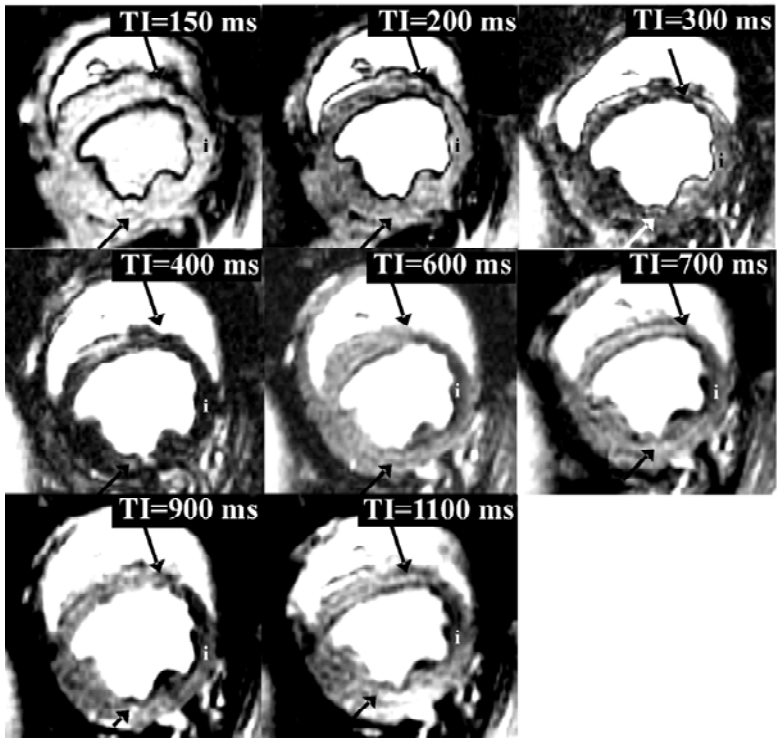

Figure 5 A representative LV images in a single slice from one dog, acquired with a series of eight TIs varying from 150 to 1100 ms. Arrows point to the edges of the ischemic region. The ischemic region is labeled with a black or white "i".

In Figure 6 the $\Delta R1_n$, WT and WM maps of the same single tomographic slice from one of the dogs are shown along with the corresponding MP. To illustrate the correspondence among the $\Delta R1_n$ map, myocardial perfusion, and the two myocardial function maps, similar colors were used for all four parameters (Fig.6).

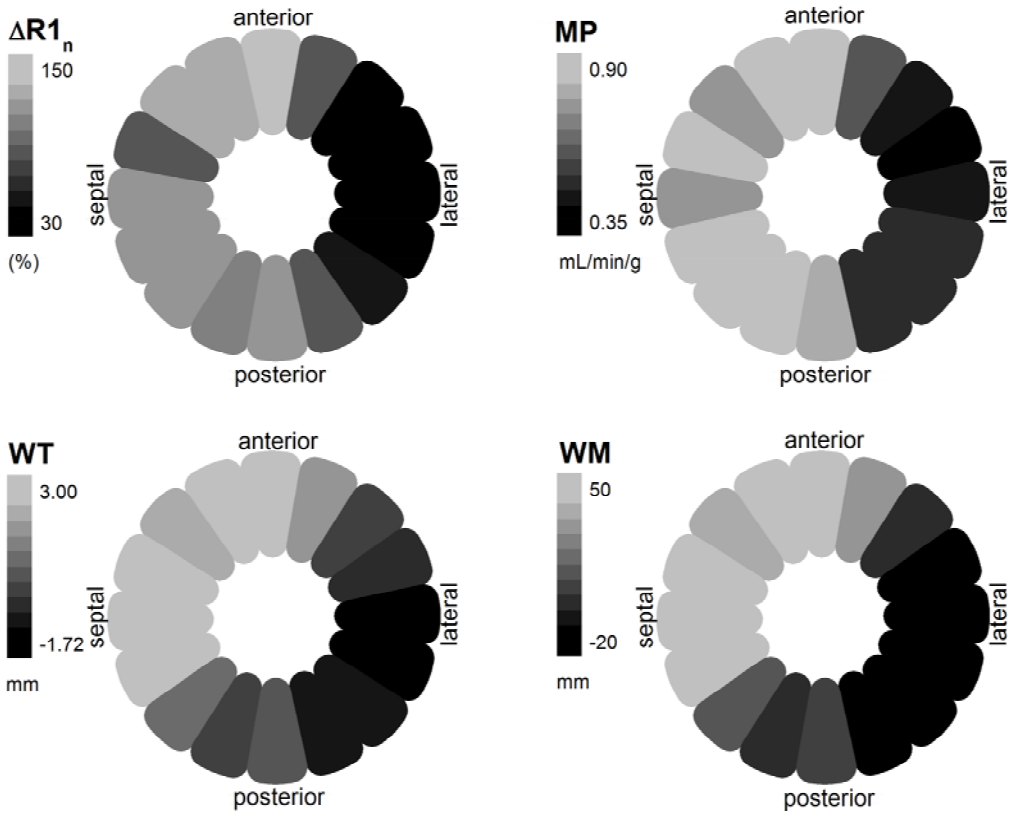

Figure 6 Each rosette illustrates one of the maps: ΔR1, MP, WT, and WM, as a function of the position of a given myocardial sector. Similar colors for all parameters were applied to emphasize the correspondence among the parameters.

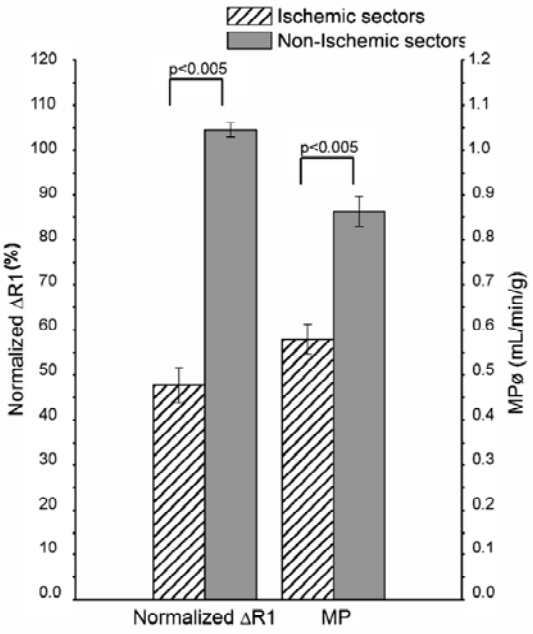

Figure 7 Average values of MP and $\Delta R1_n$ during ischemia are shown. The error bars indicate the standard error of the mean calculated by using the total number of ischemic and non-ischemic sectors.

In Fig. 7 bar graphs of the $\Delta R1_n$ values in ischemic and non-ischemic sectors from all dogs are compared with the corresponding MP bars. Mann-Whitney Rank test was used to determine the displayed p values of this comparison.

In Figure 8 the $\Delta R1_n$ data measured in the ischemic sectors of the 11 dogs are plotted as a function of the MP values in the corresponding sectors. The correlation coefficient calculated by using Pearson's Product Moment Correlation is 0.694 ($p<0.005$). Based on the correlation between $\Delta R1_n$ and MP the myocardial perfusion is calculated from the $\Delta R1_n$ values.

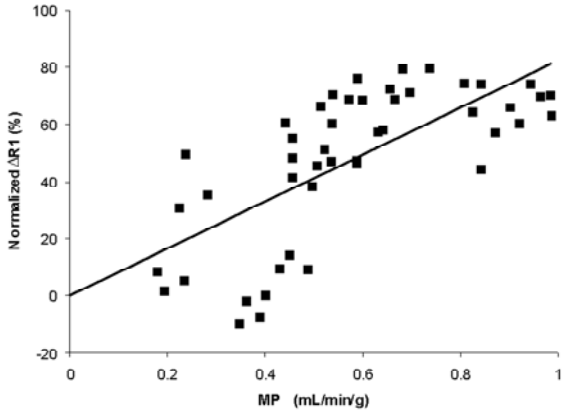

Figure 8 Normalized ΔR1 as a function of MP in all ischemic sectors evaluated in eleven dogs. The regression line was $y = 82.27x + 0.04$.

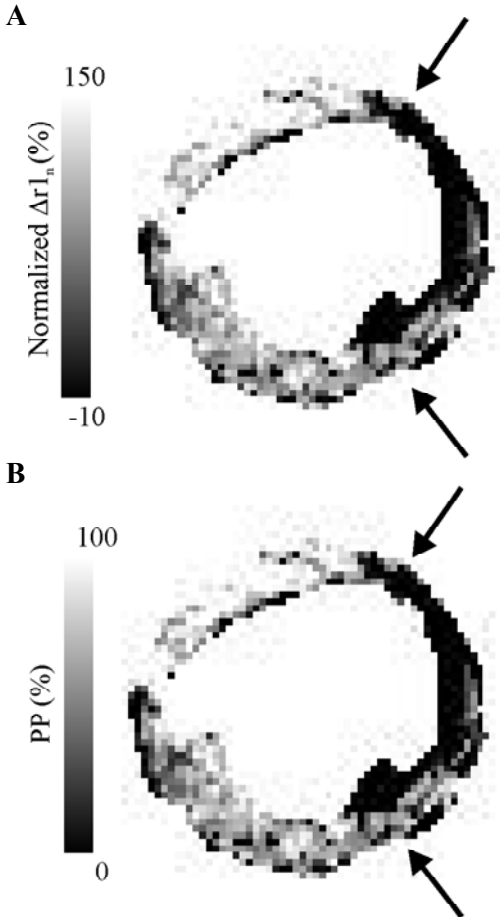

Figure 9 (A) The calculated pixel-by-pixel $\Delta R1_n$ map of the LV. The arrows indicate the edges of the ischemic zone. **Figure 9 (B)** The corresponding calculated pixel-by-pixel PPM. The arrows indicate the edges of the ischemic zone.

In Fig. 9A, the potential of the method is demonstrated by a pixel-by-pixel resolved $\Delta R1_n$ map of a single tomographic slice. Based on validation of the correlation between $\Delta R1_n$ and MP, a pixel-by-pixel Percent Perfusion Map has been calculated in the same slice, and is shown in Figure 9B.

Wall thickening (WT) and wall motion (WM) measured in the ischemic and non-ischemic sectors are shown along with the corresponding $\Delta R1_n$ and MP values in Figure 10.

Pairwise correlations were determined between $\Delta R1_n$ and WT, $\Delta R1_n$ and WM, and $\Delta R1_n$ and MP in all ischemic sectors evaluated in eleven dogs using Pearson's Product Moment Correlation. The correlation coefficients are compiled in Table 3.

Table 3. The pairwise correlation between $\Delta R1_n$, MP, WT, and WM values from all ischemic sectors evaluated in eleven dogs. The statistical parameters here were obtained by Pearson's Product Moment Correlation.

Parameters	Correlation coefficient (*R*)	p value
$\Delta R1_n$ vs. MP	0.694	P<0.005
$\Delta R1_n$ vs. WT	0.534	P<0.005
$\Delta R1_n$ vs. WM	0.529	P<0.005

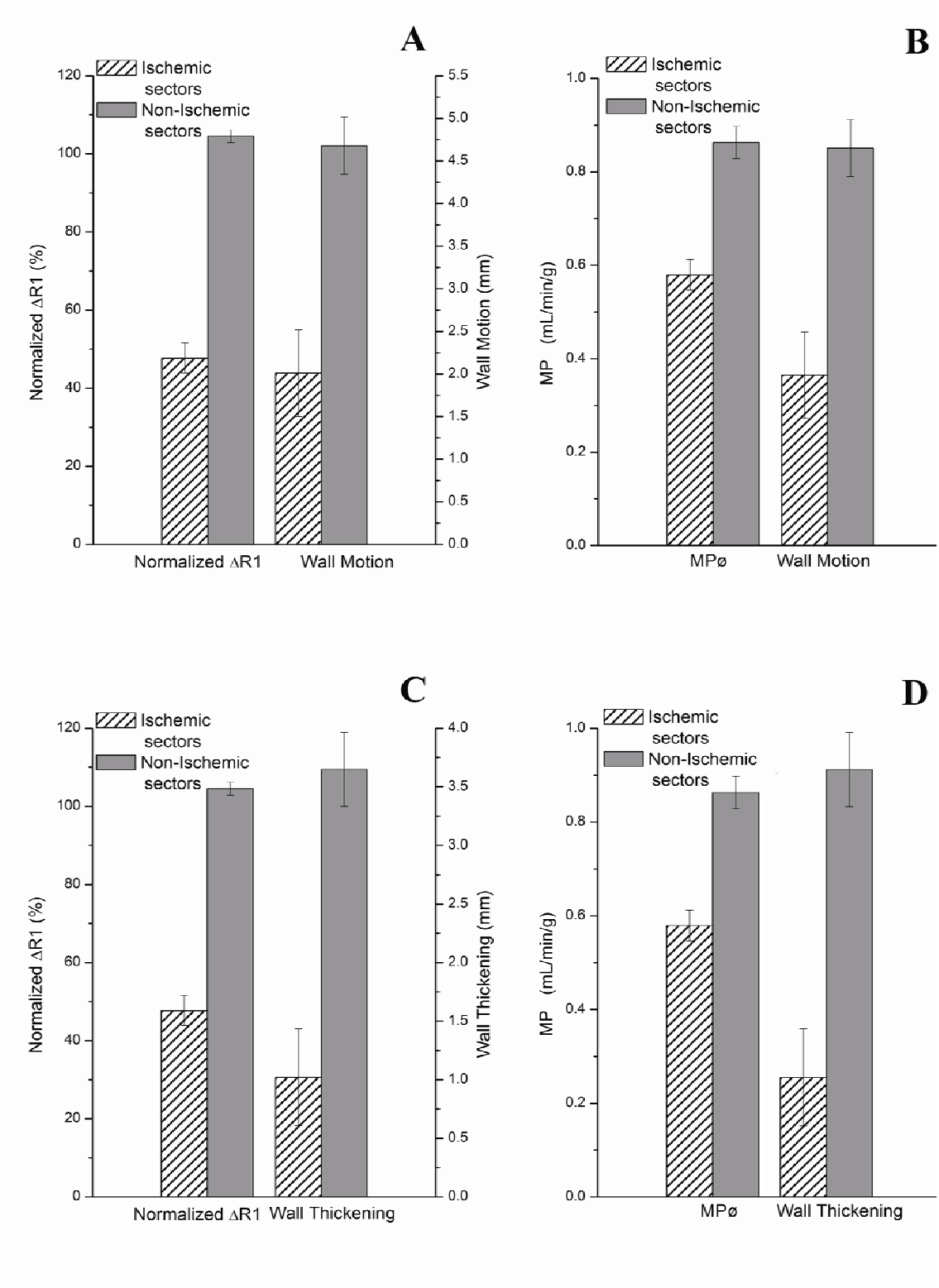

Figure10 Average values of $\Delta R1_n$ and Wall Motion (A), MP and Wall Motion (B), $\Delta R1_n$ and Wall Thickening (C), and MP and Wall Thickening (D), are shown. The error bars indicate the standard error of the mean calculated by using the total number of ischemic and non-ischemic sectors from all eleven dogs.

5.4 CONCLUSIONS

The present study demonstrates the usefulness of normalized ΔR1 mapping using Gd(ABE-DTTA) for measuring myocardial perfusion and thus quantitatively delineating the ischemic regions *in vivo*. The $\Delta R1_n$ map reflects the distribution of the CA concentration in the myocardium, and thus it is able not only to visualize, but also to quantify, the extent of ischemia in the myocardium. $\Delta R1_n$ mapping visualizes R1 increases induced by a CA more effectively than the usual T1-weighted signal intensity images. Such mapping, however, requires a contrast agent with a myocardial life-time long enough to allow the relatively long acquisitions needed for accurate determination of R1. Gd(ABE-DTTA) is a contrast agent whose sufficiently long myocardial lifetime maintains agent concentration practically unchanged in the course of a complete set of R1 acquisition. Thus using this agent it is possible to generate an accurate R1 map in a canine model of acute myocardial ischemia.

6. USING THE SAME METHOD IN A DIFFERENT DISEASE: VIRTUAL *in vivo* BIOPSY MAP OF EARLY PROSTATE NEOPLASM IN TRAMP MICE

6.1 INTRODUCTION

Prostate cancer (PC) is a commonly diagnosed cancer and the second leading cause of death in North American men.(41,42) Detecting prostate neoplasia early and providing the availability of improved prognostic tools are crucial for reducing morbidity and mortality from PC.(42)

In its initiation phase, PC is uniquely recognized as slow growing.(43-45) Autopsy studies have revealed that about 15-30% of males over the age of 45-50 have histological evidence of prostate cancer. Only in a small percentage PC becomes clinically manifest with age. PC fatalities are rarely due to primary tumors, but rather to widespread metastatic disease. Epithelial carcinogenesis proceeds via multiple steps of molecular and cellular alterations. These events can be separated into three distinct phases: initiation, promotion and progression. Mechanisms that trigger the progression of slowly growing, localized prostate tumors to a more aggressive form, and metastasis to distant organs, are poorly understood.(46) In our previous study, using MRI imaging, we showed that the expression of mutant p53 in the prostate increased the rate at which prostate tumors, initiated by SV40 Tag, progress to poorly differentiated adenocarcinoma.(47) The lack of reliable methods to track the progression of prostate cancer *in vivo* may be one reason for the lack of effective preventive and therapeutic modalities, or chemopreventive strategies for advanced PC.

Numerous prognostic markers have been developed to detect PC. Due to its controversial diagnostic value, Prostate Specific Antigen (PSA) can no longer be

considered a reliable marker of PC in its early phase. (48) (49) A new hope among biomolecular diagnostic tools is proteomic pattern analysis. (50) Such types of molecular profiling of PC, however, are still in their infancy. As with any emerging technology, many limitations must be overcome before it can be applied to clinical practice.(42) To date, none of these markers can reliably detect PC in the early phase.

Prostate Intraepithelial Neoplasia (PIN) is precancerous neoplasia of the prostate. It exists as early lesion of prostate and is well defined in TRAMP mice. In humans, PIN has recently become recognized as of paramount, early, predictive importance for PC, as aptly summarized by D.G. Bostwick (51) stating that PIN is the most likely preinvasive stage before adenocarcinoma with a high predictive value as a marker, and that most patients with PIN will develop carcinoma within 10 years.

A noninvasive method, like MRI, for the detection of such an early marker would be highly desirable. To date, however, there is no consensus in the field with regard to an appropriate MRI method for the staging of PC. Some favor MRI/MRS,(52) some favor DCE MRI, over other imaging techniques. Hara et al. successfully used Dynamic Contrast Enhanced (DCE) MRI to stage prostate cancer. (53) (54) In their study, however, they seemed to have investigated only tumors larger than 1 cm and the histological state of the tumor was not earlier than well differentiated adenocarcinoma. Moreover, this study was done on large hypertrophic prostates. As to the present state of the art of early-phase MRI diagnosis of PC, a number of investigators have questioned the usefulness of MRI: Storaas et al. could not find statistically significant advantages for tumor localization adding DCE MRI information to that obtained by T2-weighted images.(55) Allen et al could not detect microscopic lesions in patients with low risk, using MRI equipped with a body coil.(56) Ikonen et al. found the detection rate by MRI of prostate tumors smaller than

5 mm to be less than 10%.(57) Note, that all the above studies investigated PC in its adenocarcinoma phase. Visualization of PIN in humans with MRI or with any other imaging method has yet to be carried out.(51)

All these MRI efforts to date have been based on signal intensity (SI) images. In contrast enhanced MRI (ceMRI) the images show tissue differentiation, when they do, on the basis of signal intensity enhancement (SIE). SIE in ceMRI is dependent on contrast agent concentration in the prostate tissue volume element (voxel) represented by the image area in question, but not in a linear fashion. SI is not an intrinsic parameter, rather it is also dependent on the pulse sequence and acquisition parameters used. Another confounding factor is the inhomogeneity caused by the MRI coil, artificially imparting varying SIs to different parts of the prostate depending on their relative position to the coil. The intrinsic physical parameter which is enhanced in linear proportion with contrast agent concentration is the paramagnetic ΔR1 ($\Delta R1_p$) (longitudinal relaxation rate enhancement), induced by a contrast agent.(4) The $\Delta R1_p$ of a given prostate tissue volume element actually represents the $\Delta R1_p$ value integrated over that volume element, because the ΔR1, contrary to MRI SI parameters, is additive. Thus, a three dimensional (3D) R1 map of the prostate is a faithful representation of contrast agent distribution with the same in-plane resolution as of a regular image and with the slice thickness determining the resolution in the third dimension.

Our results indicate that the contrast agent Gd(ABE-DTTA) (58) is distributed in the prostate in the TRAMP mouse model in inverse proportion to the tissue's neoplastic content. It is quite evident from the state of the art that a yet nonexistent, noninvasive imaging method for repeat monitoring of PIN is highly desirable and timely. We wish to suggest such a method, ceMRI combined with our contrast agent,

Gd(ABE-DTTA), using a particularly useful method of image analysis, R1 mapping. In our study in twelve TRAMP and three control mice, we have shown that prostate tissue with early high-grade PIN and/or still well-differentiated adenocarcinoma (WD) can be distinguished by our method from normal tissue and/or low-grade PIN. The results presented here suggest a potential method for future clinical use.

6.2 METHODS

Through a concerted effort in several laboratories, Greenberg et al (61) (62) (63,64) established a transgenic mouse model of PC, TRAMP (***TRA***nsgenic ***M***ouse ***P***rostate adenocarcinoma). TRAMP mice were generated with the SV40 small and large T antigen (Tag) regulated by the rat probasin gene promoter. Since probasin is a prostate-specific protein, this provides targeted expression of Tag in the prostate, resulting in transgene expression spatially restricted to the prostate. Expression correlates with sexual maturity and is hormonally regulated by androgens. TRAMP mice display progressive forms of prostate carcinoma, with development of premalignant lesions, mouse prostate intraepithelial neoplasia (PIN), carcinoma in situ, local advancement into lymphatics, metastatic disease and androgen receptor resistance (61) (62) (63,64). Many of the biological variables that drive prostate growth and invasion have been identified in this mouse. Originally, TRAMP mice had been kindly provided by Dr. Greenberg (Baylor College of Medicine, Houston) to one of our authors, Dr. Ada Elgavish, who then established a colony of TRAMP mice at the UAB. In our study, the TRAMP mouse model was used to investigate the detection of PIN, the early, precancerous form of prostate cancer.

Contrast Agent (Gd(ABE-DTTA)

The contrast agent Gd(ABE-DTTA) was synthesized and sample preparation was carried out as described above on page 19.

Anesthesia and Contrast Agent Administration Prior to MRI Sessions

Mice were initially anesthetized using 0.15 vol% Isoflurane. The tail vein was punctured and Gd(ABE-DTTA) was administered at a dose of 0.05 μmol per gram body weight. Anesthesia was continued at the reduced dose of 0.12 vol% Isoflurane. The mouse then was placed in the MRI coil. Body temperature was maintained by a custom made electric heat blower attached to a conduit.

MRI

A 4.7T Bruker MRI scanner was used, equipped with a 78 mm diameter body coil. Following the initial setup (tuning, shimming, receiver gain setting, etc.), a quick T2-weighted image set was acquired to determine the position of the prostate. Once done, a single 2 mm thick tomographic slice, containing the entire organ and typically close to the coronal orientation with the urethra in the center, was oriented through the prostate. This slice was used to acquire the R1 map for the entire prostate volume. A Multi-Slice Multi-Echo (MSME) inversion recovery (IR) sequence was used for acquisition of R1 maps with the following parameters: FOV: 5 cm, matrix: 128·128, voxel size: 0.39mm·0.39mm·2mm, number of slices: 1, recycle time (TR): 3000 ms, inversion times (TI): 60, 100, 200, 300, 600, 800, and 1000 ms. At the end of the MRI session the mouse, still anesthetized, was euthanized using a mixture of ketamine and xylazine overdose followed by cervical dislocation.

R1 map:

The part of the image that contains both lobes of the prostate (an approximately 2.4cmx2.4cm square out of the 5cmx5cm field of view) was selected as region of interest (ROI) for analysis. This square constituted a 60 pixel by 60 pixel matrix. Since all the images of a given stack were acquired within the exact same slice and with the position of this ROI remaining constant, the eight images in a stack were of identical registration. Thus the only parameter varied among these eight images was the TI.

The R1 value of each pixel in the 60x60 pixel matrix was calculated from the SI vs. TI dependence, applying a three-parameter least-squares curve fitting routine, using the following formula (60)

$$SI = SI_o \cdot (1 - A \cdot e^{-TI \cdot R1}) \qquad \text{Eq 1}$$

where SI is the signal intensity obtained with a given TI, SI_0 is the signal intensity at equilibrium, and A is a constant which in the absence of saturation and under other ideal conditions would equal 2.0.

The R1 value in each pixel was calculated from the SI vs. TI dependence as shown above. A good image quality, necessary for accurate R1 determinations, as well as a good coregistration of all images within the same stack, was confirmed by the correlation coefficient (R^2).

R1 values estimated from SI values acquired with only two or three inversion delays are not as accurate as those measured with the eight TI inversion recovery (IR) set, which, however, is time consuming. A fast sequence approach has been recently demonstrated by Messroghli et al., showing the feasibility of fast IR-based R1 mapping of the heart in patients (65). Using such a technique in prostate MRI, once

the technique becomes commercially available, the time needed to acquire a R1 map of the entire prostate can be reduced substantially.

Normalized R1 Map and Neoplastic Index Map

It is difficult to administer an exact reproducible dose of the contrast agent in each individual mouse. Therefore, to eliminate possible differences among animals, the R1 values measured in a prostate region have been normalized to the R1 value measured in the thigh muscle ($R1_{norm}$) of the same animal. Following the administration of the contrast agent, we have observed that voxels with the lowest relaxivity ($R1_{lo}$) in a given prostate correspond with prostate regions that contain the largest amount of tissue that has histology scores 3-4 (see METHODS section). Conversely, voxels with the highest relaxivity ($R1_{hi}$) have been those that contain the least amount of tissue with scores 3-4. The relaxivity of any given voxel is thus governed by the relative proportions of tissue with scores 1-2 versus tissue with scores 3-4. Therefore the R1 value ($R1_v$) measured in any given voxel (v) in the prostate will be found on an R1 scale that ranges between $R1_{hi}$ and $R1_{lo}$. Thus the difference $\Delta_v = R1_{hi} - R1_v$ reflects the extent of neoplasticity in that voxel. When $R1_v = R1_{hi}$, Δ_v is zero, indicating no neoplasticity. When $R1_v = R1_{lo}$, Δ_v obtains its maximum value, reflecting a fully neoplastic voxel. A percent neoplastic index (NI_v) can be then calculated in every voxel v by normalizing Δ_v with the maximum range; i.e. $R1_{hi} - R1_{lo}$ (Eq 2).

$$NI_v = \frac{\Delta_v \cdot 100}{R1_{hi} - R1_{lo}} \qquad \text{Eq 2}$$

NI_v will take the value of 100% when $R1_v=R1_{lo}$ (maximum neoplasticity) and zero when $R1_v=R1_{hi}$ (fully normal tissue). Thus, by calculating the NI_v value for all voxels, the pixel-by-pixel R1 map of the prostate can be converted into a voxel-by-voxel NI map reflecting quantitatively the neoplastic content of every given voxel in the map.

Based on the NI_v value of all prostate voxels in a given prostate, the total volume of the cells with score≥3 (Neoplastic Volume, NV) can be calculated from Eqation 3:

$$NV = V_v \bullet \sum_{v=1}^{n} NI_v \qquad \text{[Eq 3]}$$

Where V_v is the voxel volume and n is the number of prostate voxels.

The NV values obtained from our experiments are compiled in Table 4.

Histological Analysis

Following euthanasia the urogenital tracts were excised *en bloc***,** pinned to a small piece of plastic foam to avoid disintegration of the sample. An approximately 4mm block was selected by recognizing and precisely following the urethra while slicing the urogenital tract ensuring that the entire prostate is contained in the physical block, corresponding to the tomographic slice. The slice was excised and further processed for histological analysis. It was frozen by immersing the block into 2-methylbutane liquid previously cooled with dry ice. The block later on was cut through the urethra and 5 μm thick slices were taken for histological analysis. The histological sections were stained using the Gömöri-Trichrome method. In the microscopic slides, the areas of the histologically homogenous regions, recognizable on the R1 maps (as well as on the normalized R1 maps), were measured and their

histological scores were determined as described by Wechter et al. (66) Noncancerous tissues were scored 1, 2, or 3, indicating healthy, low-grade PIN and high-grade PIN, respectively. Scores 4 indicated well-differentiated adenocarcinomas (66). In our mice only scant areas of poorly differentiated adenocarcinomas (score 5) were found and thus no appropriate statistics could be carried out on this type of tissue. Therefore, we have decided to exclude these areas from the study.

All areas of tissue regions with the same histological score were measured in the postmortem histological sections. Corresponding areas in the calculated R1, normalized R1, and Neoplastic Index maps were also measured. For each region with a well-defined score, a fractional neoplastic area (neoplastic area/total prostate lobe area) was calculated both in the histological sections and in the R1 map. Other MRI related parameters (normalized R1, NI) measured in the corresponding regions were exported for further analysis.

Statistical Analysis

Statistical analysis of the data was carried out using SigmaStat version 2.03 (SPSS, Inc). To compare two groups, Student's *t*-test was used if data passed the test for normal distribution. To compare several groups, One way ANOVA (for one independent variable) or two-way ANOVA (for two independent variables) were used. Pearson's correlation coefficient *r* was calculated to evaluate relationships. Rejecting the null hypothesis at $\alpha = 0.05$ with a P-value < 0.05 was interpreted to indicate a significant difference.

6.3 RESULTS

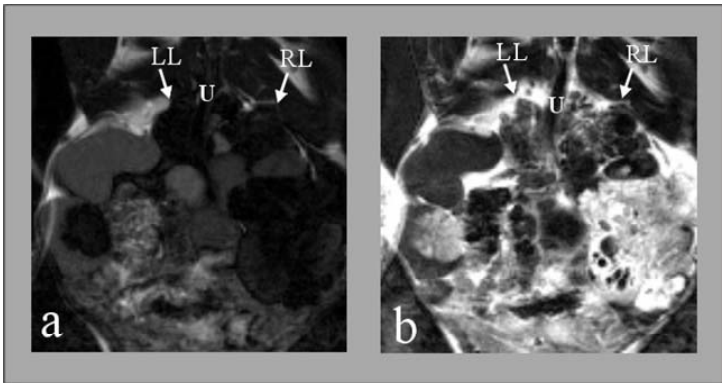

Figure11 Inversion recovery MRI images acquired with TI=800ms are shown during pre-contrast control (a), and following Gd(ABE-DTTA) administration (b). LL, RL indicate left and right lobe of the prostate, respectively and U labels the urethra.

To demonstrate the effect of the contrast agent, one inversion recovery (IR) image (at TI=800 ms) of an axial tomographic slice that contains the prostate of a TRAMP mouse is shown in Fig.11. in the absence of (a), or in the presence of (b) Gd(ABE-DTTA). In the rest of the mice similar results were obtained. In Fig.12 the corresponding R1 maps, calculated from the image sets related to the image shown in Fig.11, are shown. Although in the regular contrast enhanced, IR images (Fig.11) the prostate lobes are sufficiently delineated, no differentiation between neoplastic and normal prostate tissue is visible. Nor is such differentiation obtained in the R1 map in the absence of agent (Fig.12a). In the Gd(ABE-DTTA)-enhanced R1 image (Fig.12b), however, darker versus brighter prostate areas are evident. As proven below by comparison with histology, this R1 based differentiation in Fig.12b. corresponds to differentiation between score 3-4 neoplastic tissue versus score 1-2 tissue. Thus from comparing Figs. 11 and 12, it is

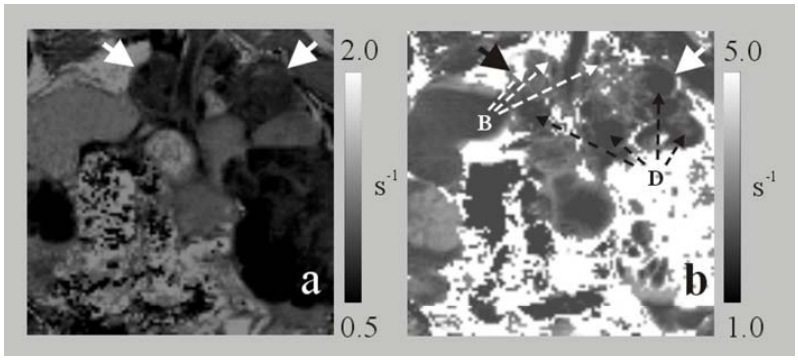

Figure12 R1 maps are shown during control (a) and following Gd(ABE-DTTA) administration (b). The thick arrows indicate the lobes of the prostate. The black broken arrows indicate the dark (D) and the white broken arrows point to the bright (B) prostate areas.

evident that only a contrast-enhanced R1 image provides diagnostically valuable information in this case. R1 mapping provides the largest contrast between healthy prostate tissue versus tissue with high-grade PIN or adenocarcinoma (Fig. 13).

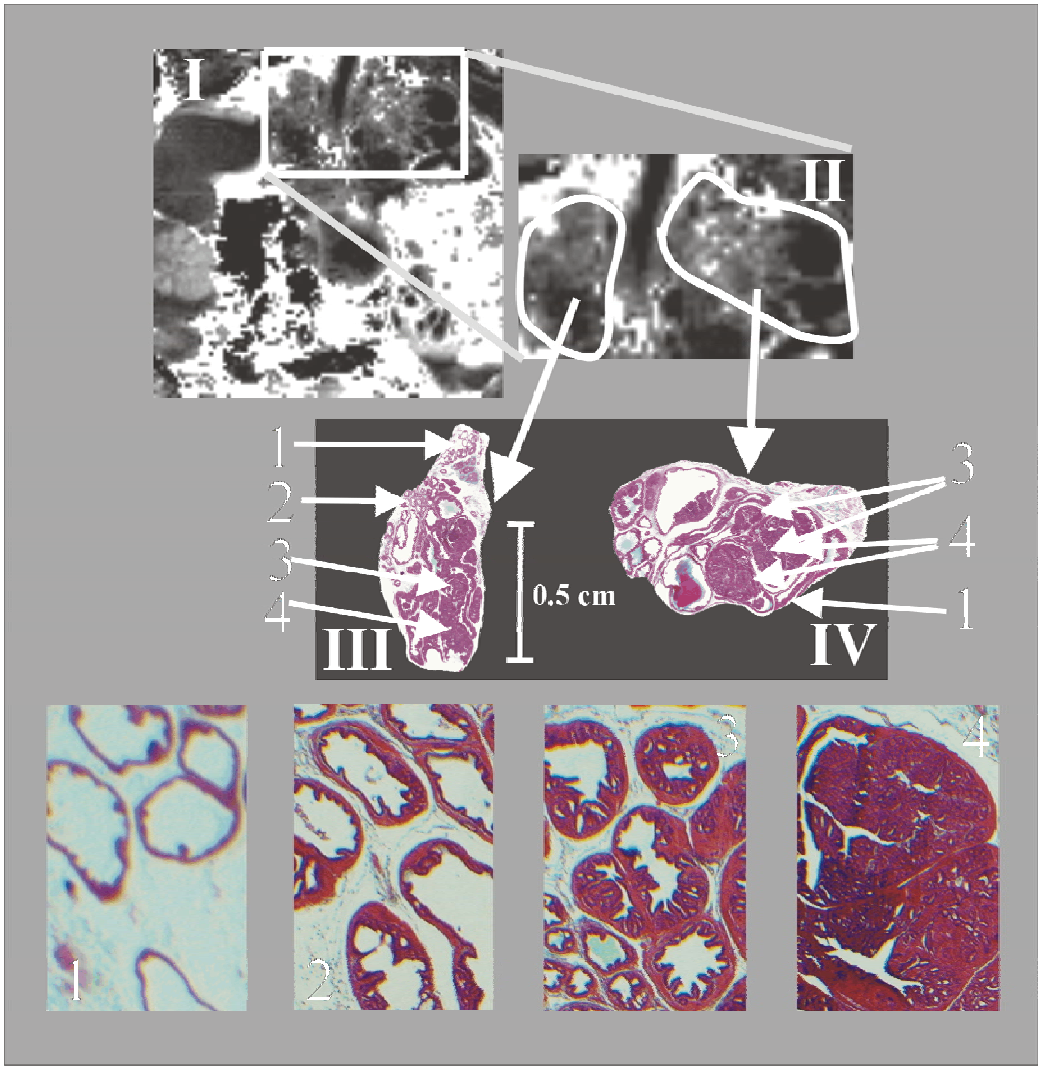

Figure13 The calculated R1 map (I), the magnified section of the prostate (II), and the histological sections of the two lobes (III-left lobe, IV-right lobe) are shown. Normal (score 1), low grade PIN (score 2), high grade PIN (score 3) and well differentiated adenocarcinoma (score 4) can be identified. The white arrows indicate the position of areas with different histological scores in the prostate tissue.

In Figure 13 the co-registration of the MRI delineated areas in the prostate lobes with the histological scores found in the corresponding physical prostate areas is shown. Wu et al (69) used three dimensional ultrasound to detect prostate tumors in TRAMP mice, but no staging of the tumors was carried out. Moreover, they couldn't

detect PIN, but only well- or poorly differentiated adenocarcinoma. The smallest tumor detected was over 3.5 mm. (69) In our present study, prostate neoplasms smaller than 2 mm could be visualized, even when consisting of high-grade PIN only and no adenocarcinoma,. The fractional neoplastic area values (see METHODS) obtained from the histological sections were correlated pairwise with values obtained from their corresponding R1 map (Fig. 14).

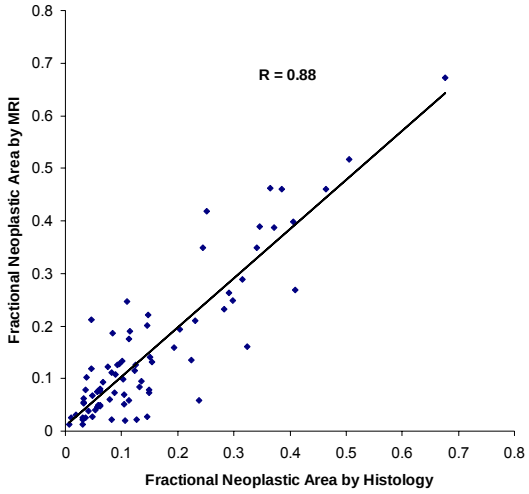

Figure14 Fractional Neoplastic Areas detected by MRI (Y axis) and Histology (X axis). The good correlation (R=0.88) indicates that the areas detected by MRI correspond well to the areas detected by histology (P<0.001)

R1 values from ROIs containing prostate tissue in the twelve TRAMP and three litter-mate nontransgenic controls were each individually normalized to the R1 in muscle tissue near the prostate of the same mouse to account for possible variations among the mice in contrast agent uptake. Mean R1(±STD) values corresponding to the histologically distinct areas were calculated first for each mouse separately and than averaged for all twelve TRAMP mice. Results were similarly calculated for the three control mice.

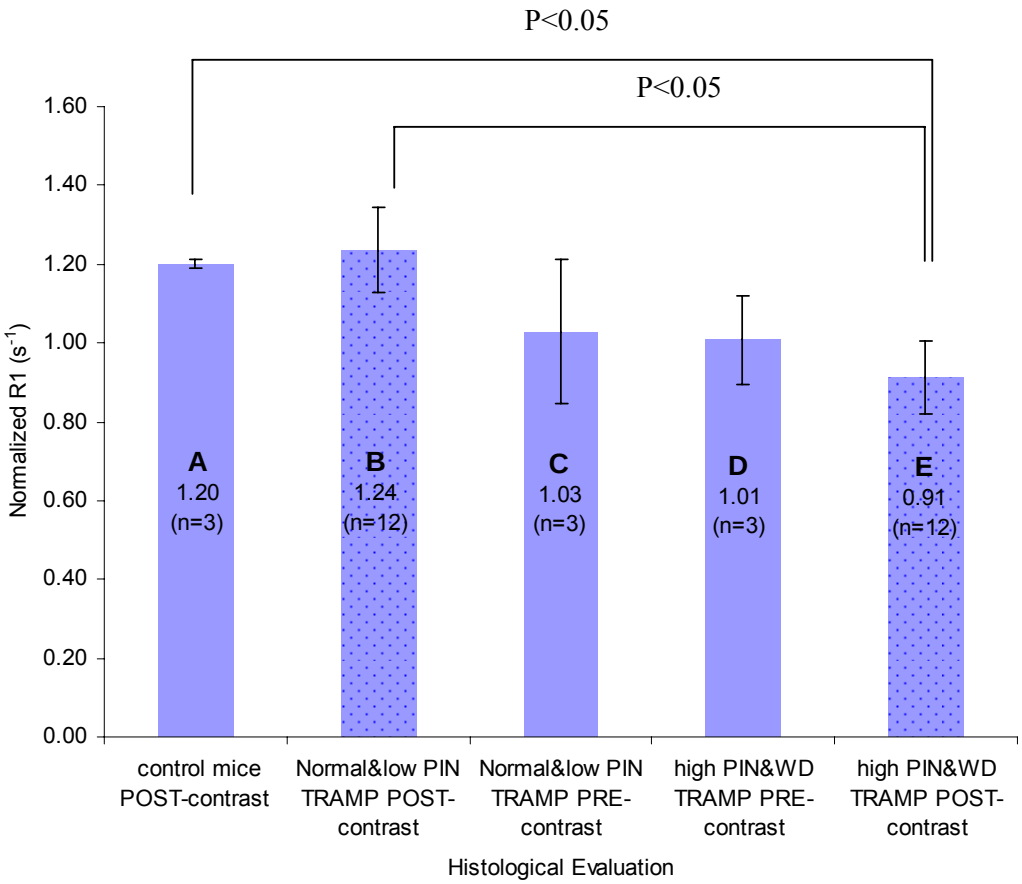

Figure15 Mean values of normalized R1 from TRAMP are shown for normal &low-grade PIN **PRE**- (1.03±0.04 s^{-1}) (**C**), and **POST**-contrast agent administration (1.24±0.03 s^{-1}) (**B**), high-grade PIN &WD **PRE**- (1.01±0.02 s^{-1}) (**D**), and **POST**-contrast (0.92±0.02 s^{-1}) (**E**), along with the overall prostate **POST**-contrast (1.20±0.01 s^{-1}) from the three control mice (**A**). As expected, the post contrast values in the control mice and the normal &low-grade PIN regions in TRAMP are practically indistinguishable, and display substantially higher post-contrast than pre-contrast values, indicating that the contrast agent is taken up into normal &low-grade PIN prostate tissue but not high-grade PIN tissue.

The overall R1 means are depicted in Figure 15 as bar graphs along with their corresponding STD values: normal&low-grade PIN **PRE**- (0.90±0.007 s^{-1}) (**C**) and **POST**-contrast agent administration (1.25±0.18 s^{-1}) (**B**), high-grade PIN&WD **PRE**- (0.88±0.02 s^{-1}) (**D**), and **POST**-contrast (0.93±0.11 s^{-1}) (**E**), along with the overall prostate **POST**-contrast from the three control mice (1.17±0.03 s^{-1}) (**A**). As expected, the post-contrast values in the control mice and the normal&low-grade PIN regions in TRAMP mice are practically indistinguishable, and substantially higher than the pre-

contrast values, indicating that the contrast agent is taken up into normal&low-grade PIN prostate tissue and persists there for the entire duration of the MRI scanning.

6.4 CONCLUSIONS

Our results indicate that Gd(ABE-DTTA) is distributed in the prostate in inverse proportion to the tissue's neoplastic content in the TRAMP mouse model. Thus, the R1 value of a given prostate volume element is governed by the fraction of neoplastic tissue of scores 3 and 4 in that volume element.

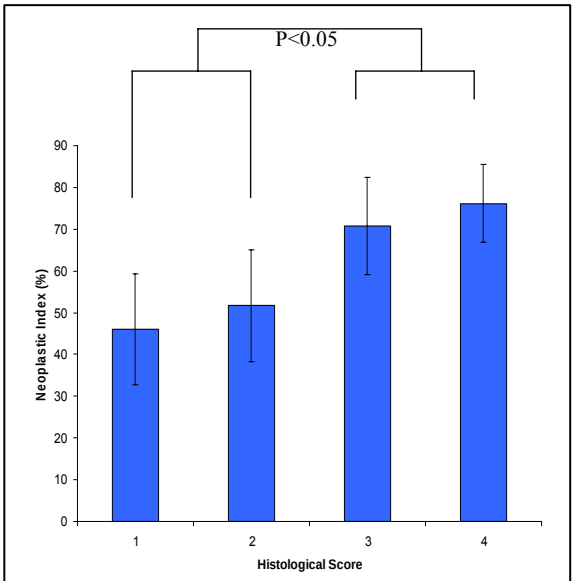

Figure16 The mean values of the Neoplastic Index (NI) shown separately for prostate regions with the different histologic scores. It is apparent that there is no statistical difference in NI between regions with scores 1 and 2 (group A), or among regions with PIN 3 and 4 (group B). There is, however, a significant difference in NI between regions from goup A versus regions from group B ($p<0.005$).

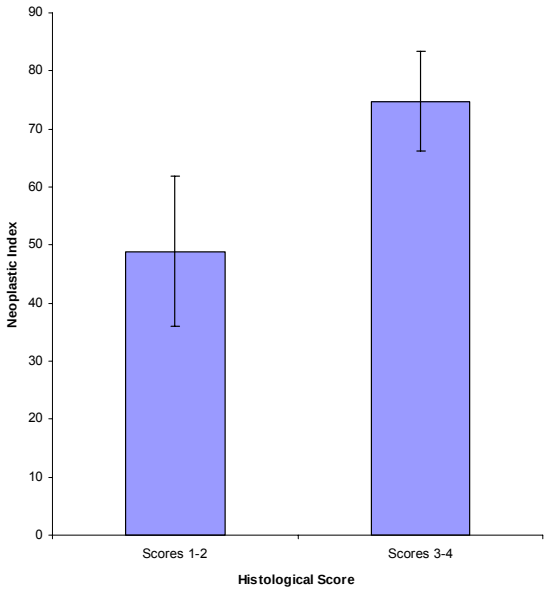

Figure17 The mean values of the Neoplastic Index found in prostate regions with scores 1and 2 (group A) versus scores 3 and 4 (group B).

Therefore, our results seem to show that an R1 map made following the administration of Gd(ABE-DTTA) can differentiate normal prostate tissue (score 1) or low score (score 2) mouse prostatic intraepithelial neoplasia (PIN) from tissues with either high score PIN (score 3) or well differentiated adenocarcinoma (WD) (score 4) within the murine prostate lobes. It is worth emphasizing that these lobes are often less than 5 mm in diameter, yet such tissue

differentiation nevertheless has been possible with our technique. Early neoplasia (scores 3-4) in a given voxel can be identified by its reduced R1 enhancement compared to normal tissue where contrast-agent induced R1 enhancement is substantially greater.

NI values (see METHODS Section) were also calculated pixel-by-pixel and were averaged in each prostate region. In Figure 16, the NI values measured in regions with different histological scores are shown. It is apparent that difference in NI from areas with score 1 versus those with score 2 does not rise to statistical significance. Similarly, the difference among the NI values from sectors with scores 3 and 4 is also non-significant. Thus, in Figure 17 we show the average NI values measured in regions with score 1-2 combined, versus regions with scores 3 and 4 combined. With the NI parameter, the difference between the two distinguishable groups of tissue areas is quite apparent. The average border value of NI for all TRAMP mice between these two groups was found to be 66.7±4.4 (see Table 4).

Table 4. Total prostate volume, mean NI ($\overline{NI_v}$), NI border values, neoplastic volume values, acquired in the twelve TRAMP mice, are shown. The lowest NI values acquired in a region with a histological score 3 or above were considered NI border values.

	Prostate Volume (uL)	$\overline{NI_v}$	NI Border Value	Neoplastic Volume (uL)
TRAMP 1	266	0.68	64	181
TRAMP 2	120	0.70	69	84
TRAMP 3	84	0.77	70	64
TRAMP 4	80	0.75	64	60
TRAMP 5	91	0.62	69	57
TRAMP 6	313	0.68	68	213
TRAMP 7	216	0.71	76	153
TRAMP 8	275	0.57	62	157
TRAMP 9	145	0.61	65	88
TRAMP 10	124	0.71	61	88
TRAMP 11	413	0.62	62	256
TRAMP 12	157	0.70	65	109

As a conclusion, a non-invasive method, using R1 mapping in the presence of Gd(ABE-DTTA) could successfully be used to distinguish early phases of prostate neoplasm from its developed phases in TRAMP mice.

7 DISCUSSION

In our work we managed to prove that Gd(ABE-DTTA) can successfully be used at high field to measure R1 and so, create R1 maps. The relaxivity of Gd(DTPA), the most often used contrast agent in the clinic, decreases with increasing field strength. Gd(ABE-DTTA), on the other hand, demonstrates a local maximum in relaxivity at a very high field strength, around 5T (Fig. 2B). As our results demonstrate, this agent can be used at any field strength between 1.5 and 10T without significant loss of efficacy.

This attribute is particularly valuable in light of the increasing field strength, to achieve better signal-to-noise ratio, of the MRI machines used in the clinic. Addition to the above detailed field dependency profile, Gd(ABE-DTTA) has a particularly long life time in the blood and in the tissues that makes this contrast agent an optimal candidate to carry out R1 measurements on the MRI instruments that currently used in the clinic.

As it was expected, in our myocardial ischemia canine experiments, based on the differential distribution of the CA in the ischemic vs. non-ischemic myocardium, the $\Delta R1_n$ values were significantly lower in the ischemic regions than in the non-ischemic areas during the ischemic period. During reperfusion, this difference vanished (Fig. 4). In the individual experiments the lower $\Delta R1$ values showed regional correlation with the regional function parameters assessed by MRI (WT, WM), as well as with the MP values (Fig. 6). A good correspondence among the various maps is evident. The underperfused areas are clearly shown by the $\Delta R1_n$ map. Good correspondence is observed between the location of the underperfused sectors defined by the $\Delta R1_n$ map and that shown by the MP map, thus validating the former.

The difference between the average $\Delta R1_n$ values measured in the ischemic vs. non-ischemic sectors is similar to that observed between the corresponding average MP values (Fig. 6).

In our experiments the ischemic areas became clearly delineated. In these areas a close correlation was found between the $\Delta R1_n$ and the MP values of the corresponding sectors (Fig. 7). A good correlation was observed between wall thickening and $\Delta R1_n$ as well as the wall motion data versus $\Delta R1_n$, demonstrating accurate localization of the ischemic regions by $\Delta R1_n$ mapping.

We have shown the extent to which the $\Delta R1_n$ values obtained after the injection of Gd(ABE-DTTA) reflect the myocardial perfusion. Once the correlation between MP and $\Delta R1_n$ has been established, a pixel-by-pixel $\Delta R1_n$ map (Fig. 8A) can be translated into a PP map with the same resolution (Fig. 8B). It is worth mentioning that with this method the spatial resolution is higher than even in the post mortem gold standard set by the microsphere determination of MP, the resolution of which is about 1 cm^3. Using the $\Delta R1_n$ map, however, each $\Delta R1_n$ value leading to the perfusion map can be obtained from a 0.014 cm^3 tomographic volume of the myocardium. Using a color scale spread between the minimum and maximum values found in the slice, the perfusion in each pixel in this calculated map can be clearly presented. The basis for these correlations is the fact that voxels with high perfusion values possess high CA concentrations, and consequently high $\Delta R1_n$ values.

Analyzing the average results of the different parameters in Figure 9, one can observe that both WT and WM show roughly proportional difference between the ischemic and non-ischemic sectors similar to those displayed by $\Delta R1_n$ and MP. As indicated by the p values (Table 1), a significant correlation was observed between

$\Delta R1_n$ and myocardial perfusion, as well as between each of the two function parameters and $\Delta R1_n$.

In clinical practice there has been a growing need for accurate and non-invasive determination of acute myocardial perfusion defects. Based on its sufficiently long myocardial lifetime, Gd(ABE-DTTA) is suitable to serve as a cardiac CA, that in conjunction with an $\Delta R1_n$ map can provide quantitative information about myocardial perfusion in ischemia.

With using our contrast agent and method (R1 mapping) we studied a model of a completely different disease, prostate neoplasm, to see if they can be used in the diagnostics of such disease as well. In the TRAMP mice experiments similar results were found.

The post-contrast mean, normalized R1 obtained from regions with high-grade PIN &WD, however, are not different from the pre-contrast mean. This suggests that high-grade PIN and WD regions did not take up Gd(ABE-DTTA), contrary to the normal&low-grade PIN regions. This indicates that a possible mechanism underlying the Gd(ABE-DTTA)-aided R1 differentiation between WD and early neoplasm (high-grade PIN) versus normal or low-grade PIN prostate tissue may be an abnormal vasculature in the neoplastic prostate areas. Such prostate vasculature has been reported by Ozawa et al. (74). Abnormal vasculature may reduce the access of the contrast agent to the high-grade PIN areas for the same reason that chemotherapeutic agents often fail to be taken up in tumors. (75)

Our results are inconsistent with the findings in human studies (53) where the post contrast MRI signal intensities were found to be higher in the cancerous areas

than in the normal prostate areas. Our results can be well understood, however, in light of the studies by Jain et al. (75). They have shown that in tumors during angiogenic development within a certain "time window", the imbalance of the pro- and anti-angiogenic (thrombobospodin-1 and VEGF, respectively) factors makes tissue blood circulation impaired due to formation of abnormal vasculature. The endothelial cells display aberrant morphology, pericytes are loosely attached or often absent, the basement membrane is also abnormal, either abnormally thick or absent. These factors lead to impaired perfusion in the tumor tissue resulting in abnormal tumor microenvironment. The hydrostatic pressure is elevated outside the blood vessel due to hypoxia and acidosis. This elevated pressure further diminishes the perfusion of the neoplastic tissues. Nevertheless, the cancer cells unfortunately can survive in such pathological microenvironment (75). Jain et al thus have suggested a new approach in cancer treatment by restoring the tumor vasculature to normal before chemotherapy by administering anti-angiogenic factors in the right period at a proper (they suggest low) dose, making the treatment more effective.(75) In short, the extensive work of Jain et al. makes our results relevant within the right period in neoplastic development while point to the possibility that human MRI studies were inadvertently carried out in a different time window.

In summary, our method is equivalent to a post-mortem biopsy examining the entire prostate, yet done noninvasively. Therefore, our method yields an *in-vivo*-obtained virtual biopsy map (VBM) (Figures 18 and 19). In this manner the 3D information inherent in MRI images can be used to quantify the extent of neoplasm. Thus, using VBM, as the only noninvasive method to date in the early phase of PC development, high-grade PIN areas and/or WD areas can be visualized in 3D with relatively high sensitivity and resolution. The practical resolution of VBM reaches

that of the MRI acquisition itself, which is higher than that of the presently used imaging techniques combined with biopsy.(76)

It is now well established that, in humans as well, PIN progresses to adenocarcinoma (77). Thus, detection of PIN could become tantamount to early detection of PC.

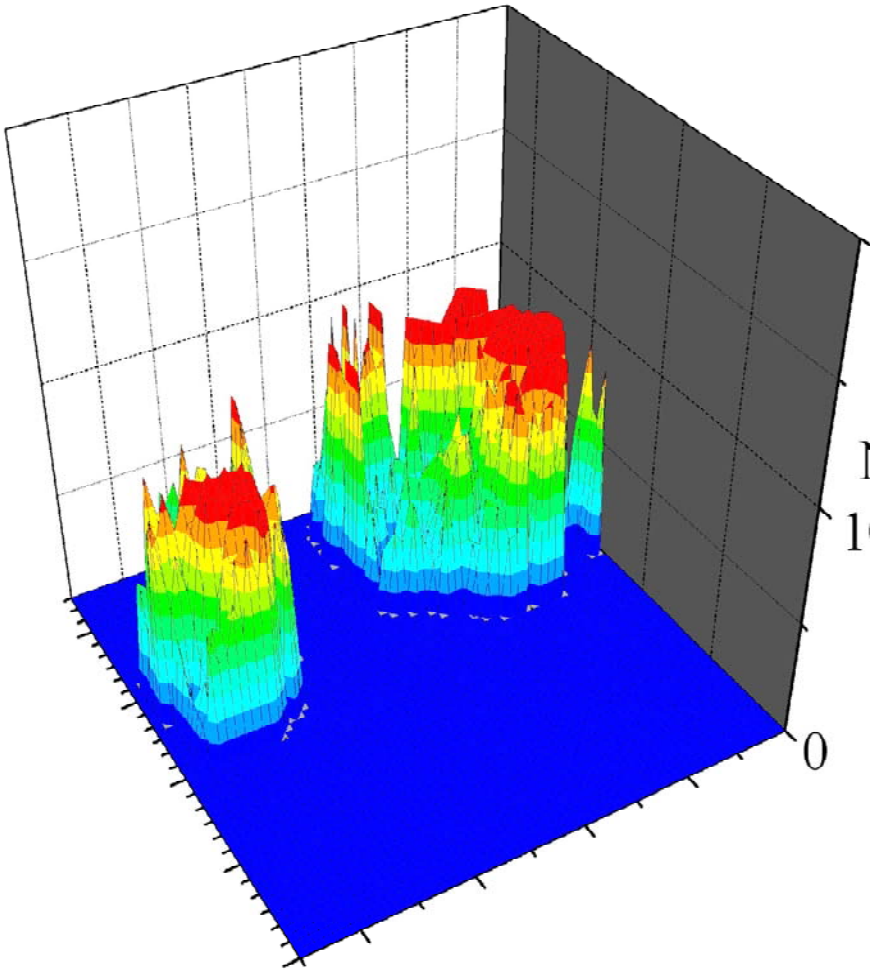

Figure18 A three-dimensional virtual biopsy map acquired from the prostate tissues of a TRAMP mouse is shown. The highest peaks highlighted with red color are the voxels with the maximum amount of tissue with scores 3 and 4. The left hand area corresponds to area III of Fig. 13, and the right hand area corresponds to area IV of Fig. 13.

Determination of NI can be utilized to predict the emergence of poorly differentiated adenocarcinoma. A high-resolution virtual biopsy map, based on this parameter, could become in the future a useful tool for clinicians in diagnosis of cancer of the prostate and possibly of other organs.

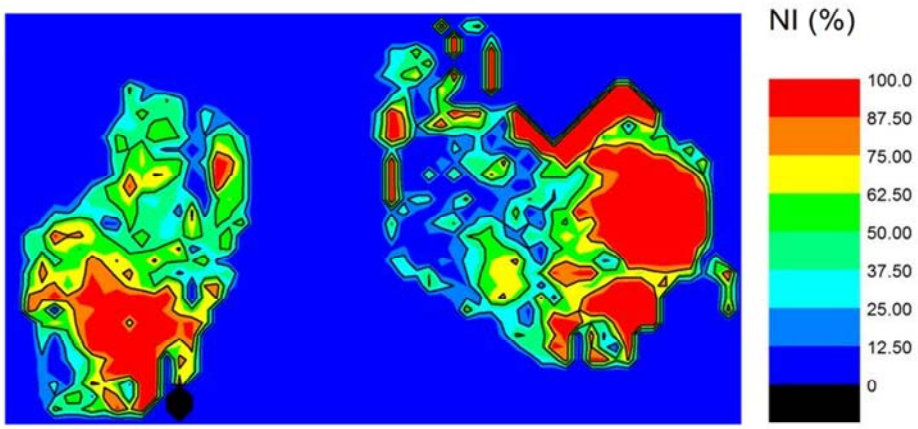

Figure19 A two-dimensional virtual biopsy map of the prostate acquired in a TRAMP mouse is shown. The red color indicates the voxels that contain the maximum amount of tissue with scores 3-4. This figure is the 2D projection of the information in Figure 18.

In conclusion, in our work we have proven in models of multiple diseases that using a contrast agent with a sufficiently long half-life and with a preserved relaxivity in the high field, R1 map can provide more, quantitative and reproducible information to the clinicians.

8 NEW FINDINGS

8.1 A unique field dependency of Gd(ABE-DTTA) was found; unlike most of the commercially available MRI contrast agents, Gd(ABE-DTTA) showed a maximum relaxivity enhancement at around 5T. This makes it suitable for using it on high field. This is an important finding considering the recent trend of the MRI instruments' field strength.

8.2 Many of the imperfections of the SI based perfusion detection in the myocardium are mostly due to the single image method itself, such as field inhomogenity, coil effects, etc. R1 measurements, however, can eliminate most of these effects. Presently, on most of the MRI instruments, the duration of an R1 measurement exceeds the half life of the commercially available contrast agents. Gd(ABE-DTTA) has a half life in the blood long enough to acquire such parameter in its present. It has successfully been used in a myocardial ischemia-reperfusion canine model to quantitatively and reproducibly detect myocardial ischemia on a voxel-by-voxel manner.

8.3 Most of the presently known MRI methods to detect human prostate neoplasm can only visualize prostate cancer in its developed phase. Using our contrast agent and the same method we successfully could detect TRAMP mouse prostate intraepithelial neoplasm in its early phase; we could distinguish mouse prostate voxels with mPIN score 1-2 from voxels with score 3 and above.

9 REFERENCES

1. Koenig S. The need for electron paramagnetic resonance and water exchange-rate data for understanding small magnetic resonance imaging contrast agents and their macromolecular complexes. Invest Radiol 1994;29 Suppl 2:S127-130.
2. Botta M. Second Coordination Sphere Water Molecules and Relaxivity of Gadolinium(III) Complexes: Implications for MRI Contrast Agents. Eur J Inorg Chem 2000;2000:399-407.
3. Liu H, Yuan L, Yang X, Wang K. La(3+), Gd(3+) and Yb(3+) induced changes in mitochondrial structure, membrane permeability, cytochrome c release and intracellular ROS level. Chem Biol Interact 2003;146(1):27-37.
4. Fritz-Hansen T, Rostrup E, Ring PB, Larsson HB. Quantification of gadolinium-DTPA concentrations for different inversion times using an IR-turbo flash pulse sequence: a study on optimizing multislice perfusion imaging. Magn Reson Imaging 1998;16(8):893-899.
5. Saab-Ismail N, Simor T, Gaszner B, Lorand T, Szollosy M, Elgavish G. Synthesis and in vivo evaluation of new contrast agents for cardiac MRI. J Med Chem 1999;42(15):2852-2861.
6. Simor T, Gaszner B, Oshinski J, Waldrop S, Pettigrew R, Horvath I, Hild G, Elgavish G. Gd(ABE-DTTA)-enhanced cardiac MRI for the diagnosis of ischemic events in the heart. J Magn Reson Imaging 2005;21(5):536-545.
7. Surányi P, Kiss P, Ruzsics B, Brott BC, Simor T, Elgavish A, Elgavish GA. Percent Infarct Mapping, a Novel In Vivo Tool for Determining Myocardial

Viability, is More Accurate than Delayed Enhancement. Proc Intl Soc Magn Reson Med 2005;13:1676.

8. Ruzsics B. Gd(ABE-DTTA), a novel contrast agent, at MRI-effective dose shows absence of deleterious physiological effects in dogs. Pharmacology 2006.

9. Yokoyama K, Nitatori T, Kanke N, Suzuki S. Efficacy of cardiac MRI in the evaluation of ischemic heart disease. Magn Reson Med Sci 2006;5(1):33-40.

10. Lombardi M, Aquaro G, Favilli B. Contrast media in cardiovascular magnetic resonance. Curr Pharm Des 2005;11(17):2151-2161.

11. Kiss P, Surányi P, Simor T, Saab-Ismail NH, Elgavish A, Hejjel L, Elgavish GA. In vivo R1-enhancement mapping of canine myocardium using ceMRI with Gd(ABE-DTTA) in an acute ischemia-reperfusion model. J Magn Reson Imaging 2006;24(3):571-579.

12. Arias E, Ph.D., and Betty L. Smith, B.S. Ed.,. Deaths: Preliminary Data for 2001. 2003;Volume 51(Number 5).

13. Schelbert H, Henning H, Rigo H, Khullar S, Ashburn W, O'Rourke R. Intravenous myocardial imaging performed serially early and late after acute myocardial infarction. Eur J Nucl Med 1977;2(2):75-83.

14. Basu S, Senior R, Dore C, Lahiri A. Value of thallium-201 imaging in detecting adverse cardiac events after myocardial infarction and thrombolysis: a follow up of 100 consecutive patients. BMJ 1996;313(7061):844-848.

15. Senior R, Glenville B, Basu S, Sridhara B, Anagnostou E, Stanbridge R, Edmondson S, Handler C, Raftery E, Lahiri A. Dobutamine echocardiography and thallium-201 imaging predict functional improvement after

revascularisation in severe ischaemic left ventricular dysfunction. Heart 1995;74(4):358-364.

16. Shiozaki H. [Diagnosis of myocardial infarction by cine MR imaging--a comparative study with thallium-201 myocardial SPECT]. Nippon Igaku Hoshasen Gakkai Zasshi 1993;53(1):11-22.

17. Sa Pinto P, Machado R, Pereira M, Almeida R, Tavares J, Rodrigues G, Matos A, Moreira A, Mendonca M, Pereira M. [Iatrogenic vascular injuries]. Acta Med Port 2000;13(1-2):39-42.

18. Alonso M, Tascon J, Hernandez F, Andreu J, Albarran A, Velazquez M. [Complications with femoral access in cardiac cathetization. Impact of previous systematic femoral angiography and hemostasis with VasoSeal-ES collagen plug]. Rev Esp Cardiol 2003;56(6):569-577.

19. Wilke N, Jerosch-Herold M, Zenovich A, Stillman A. Magnetic resonance first-pass myocardial perfusion imaging: clinical validation and future applications. J Magn Reson Imaging 1999;10(5):676-685.

20. Kraitchman D, Chin B, Heldman A, Solaiyappan M, Bluemke D. MRI detection of myocardial perfusion defects due to coronary artery stenosis with MS-325. J Magn Reson Imaging 2002;15(2):149-158.

21. Fieno DS, Shea SM, Li Y, Harris KR, Finn JP, Li D. Myocardial Perfusion Imaging Based on the Blood Oxygen Level-Dependent Effect Using T2-Prepared Steady-State Free-Precession Magnetic Resonance Imaging. Circulation 2004;110(10):1284-1290.

22. Saeed M. New Concepts in Characterization of Ischemically Injured Myocardium by MRI. Experimental Biology and Medicine 2001;226(5):367-376.

23. Al-Saadi N, Nagel E, Gross M, Bornstedt A, Schnackenburg B, Klein C, Klimek W, Oswald H, Fleck E. Noninvasive Detection of Myocardial Ischemia From Perfusion Reserve Based on Cardiovascular Magnetic Resonance. Circulation 2000;101(12):1379-1383.

24. Krombach GA, Saeed M, Higgins CB, Novikov V, Wendland MF. Contrast-enhanced MR Delineation of Stunned Myocardium with Administration of MnCl2 in Rats. Radiology 2004;230(1):183-190.

25. McNamara MT, Higgins CB, Ehman RL, Revel D, Sievers R, Brasch RC. Acute myocardial ischemia: magnetic resonance contrast enhancement with gadolinium-DTPA. Radiology 1984;153(1):157-163.

26. Schmitt M, Horstick G, Petersen S, Karg A, Hoffmann N, Gumbrich T, Abegunewardene N, Schreiber W. Quantification of resting myocardial blood flow in a pig model of acute ischemia based on first-pass MRI. Magn Reson Med 2005;53(5):1223-1227.

27. Pomeroy O, Wendland M, Wagner S, Derugin N, Holt W, Rocklage S, Quay S, Higgins C. Magnetic resonance imaging of acute myocardial ischemia using a manganese chelate, Mn-DPDP. Invest Radiol 1989;24(7):531-536.

28. Wacker C, Wiesmann F, Bock M, Jakob P, Sandstede J, Lehning A, Ertl G, Schad L, Haase A, Bauer W. Determination of regional blood volume and intra-extracapillary water exchange in human myocardium using Feruglose: First clinical results in patients with coronary artery disease. Magn Reson Med 2002;47(5):1013-1016.

29. Canet E, Janier M, Revel D. Magnetic resonance perfusion imaging in ischemic heart disease. J Magn Reson Imaging 1999;10(3):423-433.

30. Johansson L, Nolan M, Taniuchi M, Fischer S, Wickline S, Lorenz C. High-resolution magnetic resonance coronary angiography of the entire heart using a new blood-pool agent, NC100150 injection: comparison with invasive x-ray angiography in pigs. J Cardiovasc Magn Reson 1999;1(2):139-143.

31. Amano Y, Herfkens R, Shifrin R, Alley M, Pelc N. Three-dimensional cardiac cine magnetic resonance imaging with an ultrasmall superparamagnetic iron oxide blood pool agent (NC100150). J Magn Reson Imaging 2000;11(2):81-86.

32. Gerber BL, Garot J, Bluemke DA, Wu KC, Lima JA. Accuracy of contrast-enhanced magnetic resonance imaging in predicting improvement of regional myocardial function in patients after acute myocardial infarction. Circulation 2002;106(9):1083-1089.

33. Wolf G. Role of magnetic resonance contrast agents in cardiac imaging. Am J Cardiol 1990;66(14):59F-62F.

34. Atkinson D, Burstein D, Edelman R. First-pass cardiac perfusion: evaluation with ultrafast MR imaging. Radiology 1990;174(3):757-762.

35. Manning W, Atkinson D, Grossman W, Paulin S, Edelman R. First-pass nuclear magnetic resonance imaging studies using gadolinium-DTPA in patients with coronary artery disease. J Am Coll Cardiol 1991;18(4):959-965.

36. Boudraa A, Behloul F, Janier M, Canet E, Champier J, Roux J, Revel D. Temporal covariance analysis of first-pass contrast-enhanced myocardial magnetic resonance images. Comput Biol Med 2001;31(2):133-142.

37. Covarrubias DJ, Rosen BR, Lev MH. Dynamic Magnetic Resonance Perfusion Imaging of Brain Tumors. Oncologist 2004;9(5):528-537.

38. Simor T, Chu W-J, Johnson L, Safranko A, Doyle M, Pohost GM, Elgavish GA. In Vivo MRI Visualization of Acute Myocardial Ischemia and Reperfusion in Ferrets by the Persistent Action of the Contrast Agent Gd(BME-DTTA). Circulation 1995;92(12):3549-3559.

39. Simor T, Gaszner B, Saab N, Oshinski J, Waldrop S, Pettigrew R, Horvath I, Hild G, Elgavish G. Gd(ABE-DTTA)-enhanced high resolution cardiac MRI for the diagnosis of acute myocardial ischemia. XIII World Congress of Cardiology 1998:865-869.

40. Simor T, Gaszner B, Oshinski J, Waldrop S, Pettigrew R, Horvath I, Hild G, Elgavish G. Gd(ABE-DTTA)-enhanced cardiac MRI for the diagnosis of ischemic events in the heart. J Magn Reson Imaging 2005;21(5):536-545.

41. Boring CC, Squires TS, Tong T, Montgomery S. Cancer statistics, 1994. CA Cancer J Clin 1994;44(1):7-26.

42. Feroze-Merzoug F, Schober M, Chen Y. Molecular profiling in prostate cancer. Cancer Metastasis Rev 2001;20(3-4):165-171.

43. Fleshner N, Fair W. Indications for transition zone biopsy in the detection of prostatic carcinoma. J Urol 1997;157(2):556-558.

44. Cher M, Chew K, Rosenau W, Carroll P. Cellular proliferation in prostatic adenocarcinoma as assessed by bromodeoxyuridine uptake and Ki-67 and PCNA expression. Prostate 1995;26(2):87-93.

45. Dhom G. [Epidemiologic and morphogenetic aspects of prostate cancer]. Urologe A 1991;30(3 Suppl):3-4.

46. Carter H, Coffey D. The prostate: an increasing medical problem. Prostate 1990;16(1):39-48.

47. Kiss P, Lenard L., Simor, T., Forder J., Mentor-Marcel, R., Elgavish, A., Elgavish, G.A. MR Imaging As a Tool to Monitor Prostate Tumor Growth in Mice with Mutant p53 Gene.; 2001 April 21-27, 2001; Glasgow, Scotland, United Kingdom.

48. Haese A, Graefen M, Huland H, Lilja H. Prostate-specific antigen and related isoforms in the diagnosis and management of prostate cancer. Curr Urol Rep 2004;5(3):231-240.

49. Caplan A, Kratz A. Prostate-specific antigen and the early diagnosis of prostate cancer. Am J Clin Pathol 2002;117 Suppl:S104-108.

50. Conrads T, Veenstra T. The utility of proteomic patterns for the diagnosis of cancer. Curr Drug Targets Immune Endocr Metabol Disord 2004;4(1):41-50.

51. Bostwick D, Qian J. High-grade prostatic intraepithelial neoplasia. Mod Pathol 2004;17(3):360-379.

52. Rajesh A, Coakley F. MR imaging and MR spectroscopic imaging of prostate cancer. Magn Reson Imaging Clin N Am 2004;12(3):557-579, vii.

53. Hara N, Okuizumi M, Koike H, Kawaguchi M, Bilim V. Dynamic contrast-enhanced magnetic resonance imaging (DCE-MRI) is a useful modality for the precise detection and staging of early prostate cancer. Prostate 2004;62(2):140-147.

54. Noworolski S, Henry R, Vigneron D, Kurhanewicz J. Dynamic contrast-enhanced MRI in normal and abnormal prostate tissues as defined by biopsy, MRI, and 3D MRSI. Magn Reson Med 2005;53(2):249-255.

55. Storaas T, Gjesdal K, Svindland A, Viktil E, Geitung J. Dynamic first pass 3D EPI of the prostate: accuracy in tumor location. Acta Radiol 2004;45(5):584-590.

56. Allen DJ, Hindley R, Clovis S, O'Donnell P, Cahill D, Rottenberg G, Popert R. Does body-coil magnetic-resonance imaging have a role in the preoperative staging of patients with clinically localized prostate cancer? BJU Int 2004;94(4):534-538.

57. Ikonen S, Karkkainen P, Kivisaari L, Salo J, Taari K, Vehmas T, Tervahartiala P, Rannikko S. Magnetic resonance imaging of clinically localized prostatic cancer. J Urol 1998;159(3):915-919.

58. Saab-Ismail NH, Simor T, Gaszner B, Lorand T, Szollosy M, Elgavish GA. Synthesis and in vivo evaluation of new contrast agents for cardiac MRI. J Med Chem 1999;42(15):2852-2861.

59. Koenig S, Brown R. Relaxometry of magnetic resonance imaging contrast agents. Magn Reson Annu 1987:263-286.

60. Kaldoudi E, Williams SCR. Relaxation time measurements in NMR imaging. Part I: Longitudinal relaxation time. Concepts in Magnetic Resonance 1993;5:217-242.

61. Greenberg N, DeMayo F, Finegold M, Medina D, Tilley W, Aspinall J, Cunha G, Donjacour A, Matusik R, Rosen J. Prostate Cancer in a Transgenic Mouse. PNAS 1995;92(8):3439-3443.

62. Gingrich J, Barrios R, Morton R, Boyce B, DeMayo F, Finegold M, Angelopoulou R, Rosen J, Greenberg N. Metastatic prostate cancer in a transgenic mouse. Cancer Res 1996;56(18):4096-4102.

63. Gingrich J, Barrios R, Foster B, Greenberg N. Pathologic progression of autochthonous prostate cancer in the TRAMP model. Prostate Cancer Prostatic Dis 1999;2(2):70-75.

64. Kaplan-Lefko P, Chen T, Ittmann M, Barrios R, Ayala G, Huss W, Maddison L, Foster B, Greenberg N. Pathobiology of autochthonous prostate cancer in a pre-clinical transgenic mouse model. Prostate 2003;55(3):219-237.

65. Messroghli DR, Niendorf T, Schulz-Menger J, Dietz R, Friedrich MG. T1 mapping in patients with acute myocardial infarction. J Cardiovasc Magn Reson 2003;5(2):353-359.

66. Wechter WJ, Leipold DD, Murray ED, Jr., Quiggle D, McCracken JD, Barrios RS, Greenberg NM. E-7869 (R-Flurbiprofen) Inhibits Progression of Prostate Cancer in the TRAMP Mouse. Cancer Res 2000;60(8):2203-2208.

67. Koenig S, Baglin C, Brown R, Brewer C. Magnetic field dependence of solvent proton relaxation induced by Gd3+ and Mn2+ complexes. Magn Reson Med 1984;1(4):496-501.

68. Koenig S, Brown R. Relaxation of solvent protons by paramagnetic ions and its dependence on magnetic field and chemical environment: implications for NMR imaging. Magn Reson Med 1984;1(4):478-495.

69. Wu G, Wang L, Yu L, Wang H, Xuan J. The use of three-dimensional ultrasound micro-imaging to monitor prostate tumor development in a transgenic prostate cancer mouse model. Tohoku J Exp Med 2005;207(3):181-189.

70. Kellar K, Henrichs P, Spiller M, Koenig S. Relaxation of solvent protons by solute Gd3+-chelates revisited. Magn Reson Med 1997;37(5):730-735.

71. Mikawa M, Kato H, Okumura M, Narazaki M, Kanazawa Y, Miwa N, Shinohara H. Paramagnetic water-soluble metallofullerenes having the highest relaxivity for MRI contrast agents. Bioconjug Chem 2001;12(4):510-514.

72. Adzamli K, Periasamy M, Spiller M, Koenig S. NMRD assessment of Gd-DTPA-bis(methoxyethylamide), (Gd-DTPA-BMEA), a nonionic MRI agent. Invest Radiol 1999;34(6):410-414.

73. Toth E, Bolskar R, Borel A, Gonzalez G, Helm L, Merbach A, Sitharaman B, Wilson L. Water-soluble gadofullerenes: toward high-relaxivity, pH-responsive MRI contrast agents. J Am Chem Soc 2005;127(2):799-805.

74. Ozawa M, Yao V, Chanthery Y, Troncoso P, Uemura A, Varner A, Kasman I, Pasqualini R, Arap W, McDonald D. Angiogenesis with pericyte abnormalities in a transgenic model of prostate carcinoma. Cancer 2005.

75. Jain RK. Normalization of Tumor Vasculature: An Emerging Concept in Antiangiogenic Therapy. Science 2005;307(5706):58-62.

76. Zangos S, Eichler K, Engelmann K, Ahmed M, Dettmer S, Herzog C, Pegios W, Wetter A, Lehnert T, Mack M, Vogl T. MR-guided transgluteal biopsies with an open low-field system in patients with clinically suspected prostate cancer: technique and preliminary results. Eur Radiol 2005;15(1):174-182.

77. Kasper S, Smith J. Genetically modified mice and their use in developing therapeutic strategies for prostate cancer. J Urol 2004;172(1):12-19.

10 PUBLICATIONS

10.1 PAPERS – RELATED TO THESIS

1. **P. Kiss**, P. Suranyi, T. Simor, N.H. Saab-Ismail, A. Elgavish, L. Hejjel, G.A. Elgavish: *In Vivo* R1-Enhancement Mapping of Canine Myocardium Using ceMRI with Gd(ABE-DTTA) in an Acute Ischemia-Reperfusion Model. Journal of Magnetic Resonance Imaging*; J Magn Reson Imaging. 2006 Sep;24(3):571-9.* **IF: 1.651**

2. B. Ruzsics, P. Surányi, **P. Kiss**, B.C. Brott, A. Elgavish, N.H. Saab-Ismail, G.A. Elgavish: Gd(ABE-DTTA), a novel contrast agent, at the MRI-effective dose shows absence of deleterious physiological effects in dogs. *Pharmacology. 2006;77(4):188-94. Epub 2006 Jul 27.* **IF:1.019**

3. P. Surányi, **P. Kiss**, T. Simor, A. Elgavish, G.A. Elgavish: A combined method for the determination of myocardial perfusion in experimental animals using microspheres and MRI. *Journal of Cardiovascular Magnetic Resonance; 2007;9(3):549-56.* **IF:2.016**

4. P. Suranyi, **P. Kiss**, B.C. Brott, T. Simor, A. Elgavish, B. Ruzsics, N.H. Saab-Ismail, G.A. Elgavish: Percent Infarct Mapping – A R_1-map Based ceMRI Method for Determining Myocardial Viability Distribution. *Magn Reson Med. 2006 Sep;56(3):535-45.* **IF: 3.405**

5. P. Suranyi, **P. Kiss**, B. Ruzsics, B.C. Brott, T. Simor, A. Elgavish, R.A. Baker, N.H. Saab-Ismail, G.A. Elgavish: In Vivo Myocardial Tissue Kinetics of Gd(ABE-DTTA), a Tissue-Persistent Contrast Agent. *Magn Reson Med. 2007 Jul;58(1):55-64.* **IF: 3.405**

6. P. Suranyi, **P. Kiss**, B. Ruzsics, B.C. Brott, T. Simor, G.A. Elgavish: Equilibrium Signal Intensity-Mapping, an MRI Method for Fast Mapping of Longitudinal Relaxation Rates and for Image Enhancement. *Magn Reson Imaging. 2007 Jun;25(5):641-51. Epub 2006 Nov 21.* **IF: 1.672**

7. B. Ruzsics, P. Surányi, **P. Kiss,** B. C. Brott, S. Litovsky, T.S. Denney Jr, I. Aban, S.G. Lloyd, T. Simor, G.A. Elgavish, H. Gupta: Myocardial strain in sub-acute peri-infarct myocardium. *Int J Cardiovasc Imaging. 2009 Feb;25(2):151-9.* **IF: 1.268**

8. B. Ruzsics, P. Surányi, **P. Kiss,** B. C. Brott, S.S. Singh, S. Litovsky, I. Aban, S.G. Lloyd, T. Simor, G.A. Elgavish, H. Gupta: Automated multidetector computed tomography evaluation of subacutely infarcted myocardium. *J Cardiovasc Comput Tomogr. 2008 Jan;2(1):26-32. Epub 2007 Nov 19.* **IF:** not yet available

9. B. Ruzsics, P. Surányi, **P. Kiss,** B. C. Brott, A. Elgavish, T. Simor, G.A. Elgavish: Head-to-head comparison between delayed enhancement and percent infarct mapping for assessment of myocardial infarct size in a canine model. *J Magn Reson Imaging. 2008 Dec;28(6):1386-92.* **IF: 1.651**

10. **P. Kiss**, I. A. Eltoum, P. Suranyi, H. Zeng, T. Simor, A. Elgavish,G. A. Elgavish: Virtual in vivo Biopsy Map of Early Prostate Neoplasm in TRAMP Mice by MRI. *Prostate. 2009 Apr 1;69(5):449-58.* **IF:2.601**

10.2 PAPERS – NOT RELATED TO THESIS

1. I. Szokodi. F. Horkay, B. Merkely, F. Solti, L. Geller, **P. Kiss**, L. Selmeci, V. Kekesi, O. Vuolteenaho, H. Ruskoaho, A. Juhasz-Nagy, M. Toth: Intrapericardial infusion of endothelin-1 induces ventricular arrhythmias in dogs. *Cardiovascular Research. 38(2):356-64, 1998 May.* 98375058 **IF: 3.092**

10.3 SUPPLEMENTS

1. F. Horkay, I. Szokodi, B. Merkely, F. Solti, L. Geller, **P. Kiss**, L. Selmeci, I. Horvath, V. Kekesi, A. Juhasz-Nagy, M. Toth: Potential pathophysiologic role of endothelin-1 in canine pericardial fluid. *Journal of Cardiovascular Pharmacology. 31 Suppl 1:S401-2, 1998.* 98257852 **IF: 1.709**

2. I. Szokodi, F. Horkay, **P. Kiss**, L. Selmeci, I. Horvath, O. Vuolteenaho, H. Ruskoaho, A. Juhasz-Nagy, M. Toth: Characterization of canine pericardial fluid endothelin-1 levels. *Journal of Cardiovascular Pharmacology. 31 Suppl 1:S399-400, 1998.* 98257851 **IF: 1.709**

3. P. Turbucz, **P. Kiss**, F. Horkay, I. Szokodi, R. deChatel, L. Selmeci, A. Juhasz-Nagy, I. Karadi, M. Toth: High pericardial fluid levels of endothelin are not caused by altered neutral endopeptidase activity in cardiac patients. *Journal of Cardiovascular Pharmacology. 31 Suppl 1:S287-9, 1998.* 98257817 **IF: 1.709**

4. **P. Kiss**, I. Horvath, I. Szokodi, P. Toth, V. Kekesi, A. Juhasz-Nagy, M. Toth: Endothelin does not interact with angiotensin II in the coronary vascular bed of anesthetized dogs. Journal of Cardiovascular Pharmacology. *31 Suppl 1:S103-5, 1998.* 98257768 **IF: 1.709**

10.4 ORAL PRESENTATIONS

1. **P. Kiss**, P. Suranyi, T. Simor, N.H. Saab-Ismail, A. Elgavish, L. Hejjel, and G.A. Elgavish *In Vivo* T1 Mapping of Canine Hearts Using Gd(ABE-DTTA) in an Ischemia-Reperfusion Model. *Oral presentation at the Annual Meeting of The International Society for Magnetic Resonance in Medicine, Toronto, ON, Canada, July 10-16, 2003*

2. **P. Kiss,** P. Surányi, B. Ruzsics, B.C. Brott, T. Simor, and G.A. Elgavish: Ex Vivo Percent Infarct Mapping Using Gd(DTPA): R1-Based MRI Quantification of Myocardial Viability. *Oral presentation at the 14th Annual Meeting of the North American Society for Cardiac Imaging 2006, Las Vegas, Nevada, USA*

10.5 POSTER PRESENTATIONS

1. **P. Kiss**, A. Gustin, D. Buchsbaum, T. Simor, L. Lenard, S. Vickers, and G.A. Elgavish ^{19}F NMR As a Tool to Measure The Efficiency of Adenoviral CD Gene Transfer. In Vitro and In Vivo Monitoring of 5-FC to 5-FU Conversion. *Poster presentation at the Annual Meeting of The International Society for Magnetic Resonance in Medicine, Denver, CO, USA, April 1-7, 2000*

2. **P. Kiss**, L. Lenard, T. Simor, J. Forder, R. Mentor, A. Elgavish, and G.A. Elgavish MR Imaging As a Tool to Monitor Prostate Tumor Development in Mice with Mutant p53 Gene *Poster presentation at the Annual Meeting of The International Society for Magnetic Resonance in Medicine, Glasgow, Scottland, UK, April 21-27, 2001*

3. **P. Kiss**, T. Simor, L. Lenard, L. Hejjel, P. Suranyi, N.H. Saab-Ismail, and G. A. Elgavish Relaxivity of Gd(ABE-DTTA) Increases with Magnetic Field Strength Up to 5T. A Contrast Agent for High Field Imaging. *Poster presentation at the Annual Meeting of The International Society for Magnetic Resonance in Medicine, Honolulu, Hawaii, USA, May 18-26, 2002*

4. **P. Kiss**, A. Elgavish, I-E. Eltoum, P. Suranyi, H. Zeng, T. Simor, B. Ruzsics, G. A. Elgavish: Early Detection of Prostate Neoplasm Using Pixel-by-pixel R1 Mapping Following Gd(ABE-DTTA) Administration in TRAMP Mice. *Poster presentation at the 14th Annual Meeting & Scientific Sessions of International Society for Magnetic Resonance in Medicine, 2006, Seattle, Washington, USA.*

10.6 PATENT

G. A. Elgavish, P. Suranyi, T. Simor and **P. Kiss**: Differentiation of Tissue Clinical Parameters Using Nuclear Magnetic Resonance Techniques. Provisional Patent, U.S. Patent and Trademark Office No. 45,587. Docket Number **P72418US00GP**

11 ACKNOWLEDGEMENTS

I'm thankful to;

Gabriel A Elgavish, PhD for being a supportive and fair boss for many years

Tamás Simor, MD, Ph.D. for tutoring me and for being my instructor in a totally different world

Lajos Papp, MD, D.Sc. for not giving up faith in me

Erzsébet Rőth, MD, D.Sc. for her professional support and advises

Alexander Juhász-Nagy, MD, D.Sc. † for his help with my first stumbling steps in the scientific world

Ivan Horvath, MD, PhD, for his friendship and continuous support

Istvan Szokodi, MD, PhD for his help and friendship

Miklos Tóth, MD, DSc for his selfless support

I also owe my Family a lot for their tolerance for so many years.

I wish to acknowledge the tremendous help of the following personnel:

Isam A Eltoum, MD

Laszlo Hejjel, MD, PhD

Brandy Jewell

Violetta Kekesi, PhD

Attila Kovacs

Laszlo Lenard, MD, PhD

Balazs Ruzsics, MD, PhD

Pal Suranyi, MD, PhD

Eszter Szendrei

Huadong Zeng, PhD